A thin-shell two-phase microstructural model for blown film extrusion

J. C. Pirkle, Jr. and Richard D. Braatz[a)]

University of Illinois at Urbana-Champaign, 293 Roger Adams Laboratory, Box C-3, 600 South Mathews Avenue, Urbana, Illinois 61801

(Received 29 December 2008; final revision received 18 January 2010; published 14 April 2010)

Synopsis

A two-phase microstructural constitutive relation is combined with the thin-shell model for the simulation of blown film extrusion. This combination includes equations for momentum conservation, flow-enhanced crystallization, viscoelasticity, and bubble-tube cooling. Consistent with typical blown film operation, the simulations set the bubble air mass and take-up ratio as constants, while treating the machine tension and inflation pressure as dependent variables. In all the simulations performed, the high degree of crystallization, and subsequent system stiffening, located the freeze-line naturally. Bubble geometry, temperature, and crystallinity were fitted to experimental data using material and kinetic parameters mostly obtained by a simpler quasi-cylindrical model. The thin-shell microstructural model was compared to a modified quasi-cylindrical model. The models predict similar responses to operational changes, including axial locked-in stresses at the freeze-line, but have significant differences in the locked-in stresses in the transverse direction, which were attributable to the use of different momentum equations. Either model can be used for data fitting, parameter estimation, and prediction of most process responses to upsets. © *2010 The Society of Rheology.* [DOI: 10.1122/1.3366603]

I. INTRODUCTION

In blown film extrusion, molten polymer is extruded through an annular die while air is fed through an inner concentric bubble tube (Fig. 1). This internal air inflates the bubble tube, increasing its radius by stretching it in two directions: the machine (or axial) direction and the transverse direction. This action increases the bubble-tube radius and decreases film thickness. Simultaneously, the nip rolls above the die flatten the bubble and subject the film to tension in the axial (upward from the die) direction. To prevent uncontrolled bubble expansion (and possible rupture), external air supplied from a concentric outer ring begins cooling the bubble just above its extrusion from the die. The resulting temperature reduction increases the viscosity of the rising film and induces crystallization. In addition, there is a flow-induced crystallization effect. The crystallization, in turn, causes an additional increase in viscosity as the polymer solidifies. At a location known as the freeze-line height (FLH), the bubble-tube radius remains practically constant until the bubble reaches the nip rolls.

[a)]Electronic mail: braatz@uiuc.edu

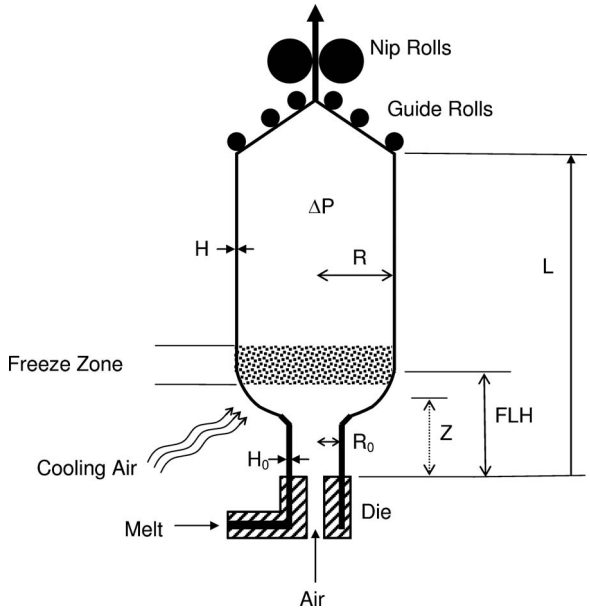

FIG. 1. Schematic of a blown film extrusion process.

A thin-shell model for steady-state blown film extrusion was first developed by Pearson and Petrie (1970a, 1970b, 1970c) and dynamic models were developed later [(Yeow (1976); Yoon and Park (1999, 2000); Pirkle and Braatz (2003); Hyun *et al.* (2004)]. In this model, most boundary conditions are specified at the inlet of the spatial domain (Z =0), which corresponds to the extrusion-die exit. One of the dependent variables, however, is the gradient of the bubble-tube radius, $y \equiv \partial R/\partial Z$, with respect to the axial direction (the longitudinal or axial gradient), and a value for this variable is unknown at Z=0. Rather, a boundary condition involving the axial gradient of the bubble-tube radius is set at the end of the spatial domain (Z=L), at the top of the bubble, and just below the nip rolls (Fig. 1). In earlier work, the boundary condition at Z=L was chosen to be $Dr/D\tau=0$, where $Dr/D\tau$ is the advection expression for the bubble-tube radius r. The resulting two-point boundary-value problem has been simulated using shooting methods, which can be numerically unstable, or finite-difference methods, which can be computationally intensive in terms of computer memory and CPU requirements. Shooting methods have been confined mostly to steady-state solutions [Han and Park (1975); Luo and Tanner (1985); Ashok and Campbell (1992)] while finite-difference methods have been used for both steady-state [Cain and Denn (1988)] and dynamic [Pirkle and Braatz (2003)] solutions. In the latter work, it was suggested that the boundary condition at Z =L not be y=0, but rather the transverse-direction momentum equation without the terms involving y. This neglect of y at Z=L is a reduced-order method [Schiesser (1996)], which leads to a smoother and more physically realistic solution.

This paper reports the parameter sensitivity analysis for a full thin-shell model that includes a two-phase microstructural constitutive model for flow-induced crystallization [Doufas and McHugh (2001); Henrichsen and McHugh (2007)] and a kinetic relation with a Gaussian dependency of crystallization kinetics on temperature [Ziabicki (1976)]. This model utilizes a single-mode Giesekus constitutive relation with transformation-dependent relaxation time, as well as a rigid rod approximation for the semi-crystalline

phase. The material properties correspond to those of a linear low-density polyethylene (LLDPE) polymer and the heat transfer coefficient has an experimentally observed spatial variation. Sensitivity analysis indicates that convective heat transfer coefficient, take-up ratio (TUR), and bubble air mass are influential controllable parameters. Material parameters of importance are those affecting crystallization rate and relaxation times of the amorphous and semi-crystalline phases.

Comparisons are made between the thin-shell model and quasi-cylindrical (QC) model [Liu (1991, 1994); Liu *et al.* (1995); Doufas and McHugh (2001); Pirkle and Braatz (2004)] when the same microstructural rheological model is used. When the two models are fit to the same experimental operating conditions, their responses to variations in TUR ratio and other operational changes at constant bubble air mass are examined. Also, comparisons are made on their sensitivities to some key material parameters.

In blown film operation, the bubble air mass is constant, after the bubble tube is inflated and the inlet air valve is shut, due to the sealing of the bubble by the nip rolls. The take-off speed V_L is set by the speed of the nip rolls. Rather than approach the blown film process by setting bubble inflation pressure and machine tension and shooting for the desired blow-up ratio (BUR), recent investigators have added the bubble air mass and TUR as constraints to the system equations [Hyun *et al.* (2004); Lee *et al.* (2006); Shin *et al.* (2007)], especially in dynamic calculations. Earlier investigators have cautioned against using inflation pressure ΔP as a set condition in modeling, as ΔP can vary widely with operating conditions at constant bubble air mass [Petrie (1975, 2002)]. This motivates the setting of the values of the bubble air mass and TUR in the simulations in this paper.

Theoretically, the thin-shell model requires two boundary conditions involving bubble-tube radius and/or its first derivative in the axial direction due to the presence of the second derivative in the momentum equation for the transverse direction. Ordinarily, the bubble-tube radius is set at the die for the first boundary condition and the second boundary condition is set at the top of the spatial domain some distance from the die and below the nip rolls. This paper will also examine both the need and the appropriate form for this boundary condition. In addition, the importance of a boundary condition at the die involving the partitioning of momentum equations into contributions from amorphous and semi-crystalline phases is examined.

II. DYNAMIC THIN-SHELL MODEL

Like the steady-state thin-shell model, the dynamic model of film motion neglects inertial terms, surface tension, drag effects of the cooling air, and gravity. The dimensional and dimensionless variables and parameters are defined in Tables I and II, respectively. The axial position Z is bounded by $Z=0$ at the die and $Z=L$ at the upper boundary of the bubble, just below the nip rolls. The freeze zone begins at the onset of crystallization and ends at the FLH, where further changes in bubble dimensions are imperceptible due to extremely large viscosity. The value of L is assumed to be sufficiently large that the bubble tube is in this frozen state well below $Z=L$.

A. Continuity and momentum equations

In the thin-shell model, the dynamic continuity equation takes the form [Yoon and Park (1999)]

TABLE I. Symbols for dimensional variables and constants.

$\mathbf{C}$	Conformation tensor, m^2
C_{pf}	Specific heat of polymer, kJ/kg K
G_{mod}	Bulk shear modulus, kPa
H_0	Film thickness as it exits die at Z=0, m
H	Film thickness at axial position Z, m
H_L	Film thickness at top boundary of freeze zone, m
k_B	Boltzmann constant
k_{crys}	Crystallization rate coefficient, 1/s
K_0	Hookean spring constant for polymer chain, N/m
L	Axial position corresponding to top boundary of bubble, m
ℓ	Length of statistical link, m
N_0	Number of statistical links in polymer chain
N_Z	Number of grid points in discretization of axial coordinate
R	Radius of film bubble tube at axial position Z, m
R_L	Final radius of film bubble tube at top boundary of bubble, m
R_0	Radius of film bubble tube as it exits die at Z=0, m
t	Time, s
T	Temperature of film bubble tube at position Z, K
T_{air}	Temperature of cooling air, K
T_∞	Equal to T_g-30, where T_g is the polymer glass transition temperature, K
T_{max}	Temperature at maximum rate of crystallization of polymer, K
T_{ref}	Reference temperature for normalization of temperature, K
T_0	Temperature of film bubble tube as it exits die at Z=0, K
U_h	Heat transfer coefficient, W/m^2 K
V	Velocity of film at axial position Z, m/s
V_L	Take-up speed of film at top boundary of bubble, m/s
V_0	Velocity of film as it exits die at Z=0, m/s
Z	Axial position measured upward from position of die, m
α_1	Adjustment coefficient for viscosity factor, Pa s
β_1	Adjustment coefficient for temperature dependence of viscosity factor, K
X	Degree of crystallinity, kg/kg
X_f	Ultimate degree of crystallinity, kg/kg
ΔH_{crys}	Heat of crystallization, kJ/kg
ΔP	Inflation pressure, relative to ambient pressure, Pa
λ_α	Relaxation time for amorphous phase, s
λ_{sc}	Relaxation time for semi-crystalline phase, s
ρ	Polymer density, kg/m^3
$\Re$	Universal gas constant, kJ/kmol K
σ_B	Stefan-Boltzmann constant
μ	Viscosity of polymer, Pa s
μ_0	Viscosity of polymer as it exits die, Pa s

$$\psi\left(h\frac{\partial r}{\partial \tau}+r\frac{\partial h}{\partial \tau}\right)+\frac{rhy}{\psi}\frac{\partial y}{\partial \tau}+rh\frac{\partial v}{\partial \varsigma}+rv\frac{\partial h}{\partial \varsigma}+hvy=0, \tag{1}$$

where

TABLE II. Symbols for variables and constants: dimensionless.

a	Dimensionless stored free energy of amorphous phase
α	Giesekus mobility parameter
BUR	Blow-up ratio=r_L
c_{ii}	ith component of the dimensionless conformation tensor $\mathbf{c}=\mathbf{C}K_0/(k_BT)$
C_{sc}	Adjustment coefficient for relaxation time of semi-crystalline phase
D_1	Dimensionless pressure force=$R_0\Delta P/[G_{mod}H0]$
D_2	Dimensionless heat transfer coefficient
D_3	Dimensionless constant for radiation in the energy equation (10)
D_4	Dimensionless constant for viscous dissipation of energy $=G_{mod}/(\rho C_{pf}T_{ref})$
D_5	Dimensionless heat of crystallization
D_x	A dimensionless constant in the crystallization equation (11)
F	Dimensionless elongational tension=$F_m-D_1r_L^2$
F_m	Dimensionless machine tension=$F_z/(\pi G_{mod}R_0H_0)$
F_{sc}	Adjustment coefficient for relaxation time of semi-crystalline phase
h	Dimensionless film thickness=H/H_0
r	Dimensionless film bubble-tube radius=R/R_0
r_L	Dimensionless film bubble-tube radius at top boundary of bubble=R/R_L
S_{ii}	Dimensionless ith component of the diagonal orientation tensor **S**
T_{ii}	Component i of dimensionless total stress tensor, normalized by G_{mod}
v	Dimensionless film velocity=V/V_0
v_L	Dimensionless take-up speed or TUR=V_L/V_0
X	Local fraction of crystallinity
X_f	Final crystallinity
ε	Emissivity for energy radiation from film
y	Dimensionless derivative of radius with respect to axial position=$\partial r/\partial \varsigma$
$\nabla\mathbf{v}$	Dimensionless velocity gradient tensor
$(\nabla\mathbf{v})_{33}$	Transverse component of the dimensionless velocity gradient tensor
ξ	Enhancement factor for crystallization
ς	Dimensionless axial position=Z/R_0
θ	Dimensionless temperature=T/T_{ref}
θ_{air}	Dimensionless temperature of air=T_{air}/T_{ref}
$\boldsymbol{\tau}_{ii}$	Component i of dimensionless extra stress tensor $\boldsymbol{\tau}$, normalized by G_{mod}
τ	Dimensionless time=tV_0/R_0
χ	Dimensionless crystallinity or extent of crystallization $=X/X_f$
ψ	Secant of angle bubble film direction makes with vertical axis=$\sqrt{1+(\partial r/\partial\varsigma)^2}$

$$\psi=\sqrt{1+y^2}, \tag{2}$$

$$y = \frac{\partial r}{\partial \varsigma}, \tag{3}$$

and r, h, v, τ, and ς are the dimensionless bubble-tube radius, film thickness, film velocity, time, and spatial position, respectively, as defined in Table II. The function ψ is the secant of the angle made by the flowing film with the vertical axis. At steady-state, Eq. (1) is readily integrated to rhv=1.

The dynamic momentum equation in the axial (or flow) direction is written in algebraic form as

$$F + D_1 r^2 - \frac{2rhT_{11}}{\psi} = 0, \tag{4}$$

where F is the dimensionless elongational tension, which is related to the dimensionless machine tension F_m by $F=F_m-D_1r_L^2$, T_{11} is the dimensionless axial (in the direction of flow) component of the total stress tensor, and D_1 is the dimensionless inflation pressure defined in Table II. The D_1r^2 term, which depends on axial position through the variable r, is the elongational stress that is due to the inflation pressure. All stress tensor components discussed in this paper, the machine tension, and the inflation pressure are normalized by the melt bulk shear modulus G_{mod}.

The dynamic momentum equation is a force balance in the direction normal to the film

$$D_1 = h\left(\frac{T_{33}}{r\psi} - \frac{T_{11}(\partial y/\partial \varsigma)}{\psi^3}\right), \tag{5}$$

where T_{33} is the dimensionless transverse component of the total stress tensor.

The boundary conditions for the thin-shell model have been the subject of some discussion. At the die, the three boundary conditions for bubble-tube radius, film thickness, and film velocity are

$$r = 1 \quad \text{at} \quad \varsigma = 0, \tag{6}$$

$$h = 1 \quad \text{at} \quad \varsigma = 0, \tag{7}$$

$$v = 1 \quad \text{at} \quad \varsigma = 0, \tag{8}$$

respectively.

For the axial gradient of the bubble-tube radius y, the boundary condition that yielded the best agreement with experiment was [Pirkle and Braatz (2003)]

$$D_1 - h\frac{T_{33}}{r\psi} = 0 \quad \text{at} \quad \varsigma = L/R_0. \tag{9}$$

This outflow boundary condition results from dropping the term containing $\partial y/\partial \varsigma$ in Eq. (5). Equation (9) is called a "minimum-order reduction" boundary condition by Schiesser (1996), who argued that such an outflow boundary condition produces more physical meaningful results than alternatives.

B. Energy and rate of crystallization equations

The energy and crystallization equations are

$$\frac{\partial\theta}{\partial\tau}+\frac{\mathrm{v}}{\psi}\frac{\partial\theta}{\partial\varsigma}+\mathrm{D}_2\frac{(\theta-\theta_{\mathrm{air}})}{\mathrm{h}}+\frac{\mathrm{D}_3(\theta^4-\theta_{\mathrm{air}}^4)}{\mathrm{h}}-\mathrm{D}_4(\tau{:}\nabla\mathrm{v})-\mathrm{D}_5\mathrm{D}_{\mathrm{x}}\mathrm{F}_\theta(1-\chi)\exp(\xi\mathrm{a})=0, \tag{10}$$

$$\frac{\partial\chi}{\partial\tau}+\frac{\mathrm{v}}{\psi}\frac{\partial\chi}{\partial\varsigma}-\mathrm{D}_{\mathrm{x}}\mathrm{F}_\theta(1-\chi)\exp(\xi\mathrm{a})=0, \tag{11}$$

where

$$\mathrm{D}_2=\frac{\mathrm{R}_0\mathrm{U}_{\mathrm{h}}}{\rho\mathrm{C}_{\mathrm{pf}}\mathrm{V}_0\mathrm{H}_0}, \tag{12}$$

$$\mathrm{D}_3=\frac{\mathrm{R}_0\sigma_{\mathrm{B}}\varepsilon\mathrm{T}_{\mathrm{ref}}^3}{\rho\mathrm{C}_{\mathrm{pf}}\mathrm{V}_0\mathrm{H}_0}, \tag{13}$$

$$\mathrm{D}_5=\frac{\Delta\mathrm{H}_{\mathrm{crys}}\mathrm{X}_{\mathrm{f}}}{\mathrm{C}_{\mathrm{pf}}\mathrm{T}_{\mathrm{ref}}}, \tag{14}$$

$$\mathrm{D}_{\mathrm{x}}=\frac{\mathrm{R}_0\mathrm{k}_{\mathrm{crys}}}{\mathrm{V}_0}. \tag{15}$$

In Eqs. (10) and (11), the exponential involving the dimensionless amorphous stored free energy a, normalized by $\mathrm{G}_{\mathrm{mod}}$, enhances the crystallization rate. For the Giesekus rigid-rod approximation, the evolution equation for the stored free energy a is [Henrichsen (2006)]

$$\frac{\partial\mathrm{a}}{\partial\tau}+\frac{\mathrm{v}}{\psi}\frac{\partial\mathrm{a}}{\partial\varsigma}=\frac{1}{1-\chi}\mathbf{c}{:}\boldsymbol{\nabla}\mathbf{v}-\frac{\mathrm{a}}{\mathrm{De}_{\mathrm{a}}(\chi,\theta)}, \tag{16}$$

where the Deborah number for the amorphous phase, De_{a}, is given in Eq. (28) and $\mathbf{c}$ is the dimensionless conformation tensor given in Eq. (31).

In Eq. (10), the first heat-loss term takes the form of Newton's law of convective cooling. The second heat loss term is due to radiation and is expected to be about 20% of that due to convection [Petrie (1974)]. Heat generation by viscous dissipation is modest under most conditions of blown-film extrusion, but it is noticeable in high stress conditions and so is included. The last term is the heat generation due to crystallization. The function F_θ is the temperature-dependent factor for the rate of crystallization and is given by the Gaussian-type function

$$\mathrm{F}_\theta=\exp\left(-\frac{(\theta-\theta_{\max})^2}{(\Delta\theta)_{\mathrm{crys}}^2}\right), \tag{17}$$

where

$$\theta_{\max}=\mathrm{T}_{\max}/\mathrm{T}_{\mathrm{ref}}, \tag{18}$$

$$(\Delta\theta)_{crys} = D_{crys}/T_{ref}, \tag{19}$$

where T_{max} is the temperature at which F_θ reaches a maximum, D_{crys} is the width of the Gaussian curve at a rate half the maximum of F_θ, and T_{ref} is the reference temperature used for normalization (usually set to the extrusion temperature). The temperature and degree of crystallization are specified at the die

$$\theta = 1 \quad \text{at} \quad \varsigma = 0, \tag{20}$$

$$\chi = 0 \quad \text{at} \quad \varsigma = 0. \tag{21}$$

For closure, the dimensionless total stress tensor components, T_{11} and T_{33}, must be defined by appropriate equations. Before doing this, it is necessary to discuss the constitutive relation for the polymer.

III. CONSTITUTIVE RELATION

Doufas and McHugh (2001) proposed a microstructural constitutive relation to describe the rheology of the polymer film during the blown film process. This relation expresses the stress-strain behavior of the polymer in terms of structural characteristics of two phases: the amorphous (or melt) phase and the semi-crystalline phase. Two key features of the relationship are the relaxation times of the amorphous and semi-crystalline phases, which depend on the viscosity of the amorphous melt, the crystallinity of the flowing film, and the bulk shear modulus. The viscosity is expressed as

$$\mu(\theta) = \alpha_1 \exp(B_1/\theta), \tag{22}$$

where

$$B_1 = \beta_1/T_{ref}, \tag{23}$$

where β_1 is the activation energy of the viscosity and α_1 is a pre-exponential factor. Conventionally, the amorphous-phase relaxation time is defined as

$$\lambda_{a,0}(\theta) = \frac{\mu(\theta)}{G_{mod}} = B_2 \exp(B_1/\theta), \tag{24}$$

where G_{mod} is the bulk shear modulus of the melt and

$$B_2 = \frac{\alpha_1}{G_{mod}}. \tag{25}$$

As crystallization occurs, the amorphous-phase relaxation time behaves as [Doufas and McHugh (2001)]

$$\lambda_a(\chi,\theta) = \lambda_{a,0}(\theta)(1-\chi)^2 \tag{26}$$

and the relaxation time of the semi-crystalline phase as

$$\lambda_{sc}(\chi,\theta) = C_{sc}\lambda_{a,0}(\theta)\exp(F_{sc}\chi), \tag{27}$$

where C_{sc} and F_{sc} are adjustable constants that are used to fit data. The relaxation times can be normalized with respect to the nominal residence time of the film, R_0/V_0.

For notational purposes, three dimensionless functions involving the relaxation times are defined as

$$De_a(\chi,\theta) = \frac{V_0\lambda_a(\chi,\theta)}{R_0}, \tag{28}$$

$$\mathrm{De_{sc}}(\chi,\theta)=\frac{\mathrm{V_0}\lambda_{\mathrm{sc}}(\chi,\theta)}{\mathrm{R_0}}, \tag{29}$$

$$\mathrm{D_s}(\chi,\theta)=\frac{\sigma_{\mathrm{drag}}}{\mathrm{De_{sc}}(\chi,\theta)}, \tag{30}$$

where σ_{drag} is the anisotropic drag parameter, $\mathrm{De_{sc}}$ is the Deborah number of the semi-crystalline phase, and $\mathrm{D_s}$ is the anisotropic drag parameter divided by $\mathrm{De_{sc}}$.

In the Doufas–McHugh microstructural model [Doufas *et al.* (2000)], the polymer melt exiting the die is a concentrated suspension of nonlinear elastic dumbbells. Each of the polymer chains is assumed to contain $\mathrm{N_0}$ flexible statistical links of length ℓ. There are two tensors that play important roles in describing polymer structure. These are the conformation tensor, $\mathbf{C}\equiv\langle\mathbf{RR}\rangle$, where $\mathbf{R}$ is the end-to-end vector of the polymer chains [Bird *et al.* (1987)], and the orientation tensor $S\equiv\langle\mathbf{uu}\rangle-(1/3)\boldsymbol{\delta}$, where $\mathbf{u}$ is the unit vector along the rod axis and $\boldsymbol{\delta}$ is the identity tensor. The brackets in the definitions of $\mathbf{C}$ and $\mathbf{S}$ indicate averaging with respect to the distribution function of the melt phase.

The evolution of the dimensionless conformation tensor $\mathbf{c}$ is governed by

$$\frac{\partial \mathrm{c_{ii}}}{\partial\tau}=-\frac{\mathrm{v}}{\psi}\frac{\partial \mathrm{c_{ii}}}{\partial\varsigma}+2(\nabla\mathbf{v})_{\mathrm{ii}}\mathrm{c_{ii}}-\frac{1}{\mathrm{De_a}(\chi,\theta)}(1-\chi)\left[(1-\alpha)+\frac{\alpha\mathrm{E_0}}{1-\chi}\mathrm{c_{ii}}\right]\left[\frac{\mathrm{E_0}}{1-\chi}\mathrm{c_{ii}}-1\right], \tag{31}$$

where $\mathrm{c_{ii}}$ is the ith component of the diagonal tensor and the components of the velocity gradient tensor, which is diagonal, are

$$(\boldsymbol{\nabla}\mathbf{v})_{11}=\frac{\mathrm{y}\dfrac{\partial \mathrm{y}}{\partial\tau}}{\psi^2}+\frac{\dfrac{\partial \mathrm{v}}{\partial\varsigma}}{\psi}, \tag{32}$$

$$(\boldsymbol{\nabla}\mathbf{v})_{22}=\frac{1}{\mathrm{h}}\frac{\partial \mathrm{h}}{\partial\tau}+\frac{\mathrm{v}}{\mathrm{h}\psi}\frac{\partial \mathrm{h}}{\partial\varsigma}, \tag{33}$$

$$(\boldsymbol{\nabla}\mathbf{v})_{33}=\frac{1}{\mathrm{r}}\frac{\partial \mathrm{r}}{\partial\tau}+\frac{\mathrm{vy}}{\mathrm{r}\psi}. \tag{34}$$

Henrichsen (2002) found that setting the nonlinear force factor E to a constant $\mathrm{E_0}$ simplified the computational procedure without causing appreciable error and that setting the isotropic drag parameter σ_{drag} to a value around 0.5 to 1.0 had a negligible effect. To compare our results to those of Henrichsen and McHugh (2007), this approximation is incorporated into subsequent equations. Alternative approaches to the approximation of E have been combined with the original Doufas–McHugh model [Doufas and McHugh (2001)], such as that of Patel *et al.* (2008) which accounts for cases where $\mathrm{N_0}$ is small (can be on order of 25 for polyolefin melts).

After the onset of crystallization, Eq. (31) still holds and the evolution of the orientational tensor $\mathbf{S}$ is given by

$$\frac{\partial S_{ii}}{\partial \tau} = -\frac{v}{\psi}\frac{\partial S_{ii}}{\partial \varsigma} + \left\{ 2\left(S_{ii} + \frac{1}{3}\right)(\nabla \mathbf{v})_{ii} - D_s(\chi,\theta)S_{ii} - 2(1-w)\left[\frac{2}{15}(\nabla \mathbf{v})_{ii} + \frac{1}{7}(DVS + 4(\nabla \mathbf{v})_{ii}S_{ii})\right] - 2w(DVS)\left(S_{ii} + \frac{1}{3}\right)\right\}, \tag{35}$$

where S_{ii} is the ith component of $\mathbf{S}$, which is diagonal. The definition of w is

$$w = 1 - 27\left(S_{11} + \frac{1}{3}\right)\left(S_{22} + \frac{1}{3}\right)\left(S_{33} + \frac{1}{3}\right) \tag{36}$$

and DVS is defined as

$$DVS = (\nabla \mathbf{v})_{11}S_{11} + (\nabla \mathbf{v})_{22}S_{22} + (\nabla \mathbf{v})_{33}S_{33}. \tag{37}$$

Only the components for i=1 and 3 must be computed as $\mathbf{S}$ has zero trace and $S_{22} = -S_{11} - S_{33}$.

Once crystallization is appreciable, which is just above the die with the Gaussian kinetic model, the extra-stress tensor components are given by

$$\tau_{ii} = \frac{E_0 c_{ii}}{1-\chi} - 1 + 3S_{ii} + 6De_{sc}(\chi,\theta)\left\{(1-w)\left[\frac{2}{15}(\nabla \mathbf{v})_{ii} + \frac{1}{7}(DVS + 4(\nabla \mathbf{v})_{ii}S_{ii})\right] + w(DVS) \times \left(S_{ii} + \frac{1}{3}\right)\right\}. \tag{38}$$

The two components, T_{11} and T_{33}, of the dimensionless total stress tensor required in the momentum equations, Eqs. (4) and (5), are calculated from the extra-stress tensor as

$$T_{11} = \tau_{11} - \tau_{22}, \tag{39}$$

$$T_{33} = \tau_{33} - \tau_{22}. \tag{40}$$

The random coil configuration is assumed in the film-thickness direction at $\varsigma=0$ [Doufas and McHugh (2001)] so

$$c_{22} = \frac{1}{E_0} \tag{41}$$

holds at $\varsigma=0$ for all times. To account for the inclusion of the rigid rod approximation at the die, previous investigators [Henrichsen *et al.* (2004); Henrichsen (2006); Henrichsen and McHugh (2007)] split the momentum equations into amorphous and semi-crystalline components. Applying their approach yields four equations at $\varsigma=0$, which can be solved for $c_{11,0}$, $c_{33,0}$, $S_{11,0}$, and $S_{33,0}$. To do this, first partition the extra-stress tensor $\boldsymbol{\tau}$ as

$$\tau_{ii(a)} = \frac{E_0 c_{ii}}{1-\chi} - 1, \tag{42}$$

$$\tau_{ii(sc)} = 3S_{ii} + 6De_{sc}\left\{(1-w)\left[\frac{2}{15}(\nabla \mathbf{v})_{ii} + \frac{1}{7}(DVS + 4(\nabla \mathbf{v})_{ii}S_{ii})\right] + w(DVS)\left(S_{ii} + \frac{1}{3}\right)\right\}. \tag{43}$$

Then substitute Eqs. (6), (7), (21), and (42) into Eqs. (4) and (5) at $\varsigma=0$ to give

$$F + D_1 - \frac{2E_0(c_{11,0} - c_{22,0})}{\psi} = 0, \tag{44}$$

$$D_1 + \left[\frac{E_0(c_{11,0} - c_{22,0})(\partial y/\partial \varsigma)}{\psi^3} - \frac{E_0(c_{33,0} - c_{22,0})}{\psi} \right] = 0. \tag{45}$$

This leads to the expressions

$$\frac{2(\tau_{11(sc)} - \tau_{22(sc)})}{\psi} = 0, \tag{46}$$

$$\frac{\tau_{33(sc)} - \tau_{22(sc)}}{\psi} - \frac{(\tau_{11(sc)} - \tau_{22(sc)})(\partial y/\partial \varsigma)}{\psi^3} = 0, \tag{47}$$

where r and h have been set to unity at $\varsigma = 0$. The amorphous phase has the responsibility of obeying the momentum equations as only amorphous material exits the die. Equations (46) and (47) assume that the semi-crystalline phase asymptotically approaches zero in the limit as ς goes to zero. This leaves only the velocity gradient tensor $\nabla \mathbf{v}$ at $\varsigma = 0$ to be specified. At steady-state, only $dr/d\varsigma$ and $dh/d\varsigma$ at the die need to be specified and Henrichsen and McHugh (2007) found that computed results were insensitive to reasonable guesses of these gradients. Using a dynamic model avoids having to guess $\nabla \mathbf{v}$ at $\varsigma = 0$, as discussed in Sec. V.

IV. OPERATIONAL CONSTRAINTS

In generating solutions to the above differential-algebraic equation (DAE) system, the bubble air mass M_{air} and the take-up speed V_L need to be set. Two equations are added to those already presented

$$M_{air} = \frac{(P_{atm} + \Delta P)}{\Re T_{air}} R_0^3 \pi \int_0^{R_0/L} r^2 d\varsigma \quad \text{as} \quad \tau \to \infty \tag{48}$$

and

$$TUR = V_L/V_0 = v_L \quad \text{as} \quad \tau \to \infty, \tag{49}$$

where M_{air} is the steady-state bubble air mass, P_{atm} is the atmospheric pressure, $\Re$ is the universal gas constant, and TUR is the steady-state TUR.

With the addition of Eqs. (48) and (49), two new variables need to be added to keep the DAE system well-posed. These are the former parameters F and D_1, which are now treated as dependent variables so that the new augmented set of equations is obeyed. The initial conditions for F and D_1 are

$$F = 0 \quad \text{at} \quad \tau = 0, \tag{50}$$

$$D_1 = 0 \quad \text{at} \quad \tau = 0, \tag{51}$$

which evolve over time to their steady-state values.

V. NUMERICAL METHODS OF SOLUTION

The numerical method of lines [Schiesser (1991)] was used to solve the partial differential-algebraic system. The equations were discretized with respect to the spatial variable ς at a number of grid points N_Z. Spatial derivatives such as $\partial v/\partial \varsigma$ were approximated as five-point finite differences in order to achieve fourth-order accuracy, thus eliminating the spatial variable as an independent variable. A variable-grid spacing technique was used as coded in the subroutine DSS032 [Silebi and Schiesser (1992)]. Spatial

derivatives were approximated by using five-point biased upwind differences for $\partial r/\partial \varsigma$, $\partial h/\partial \varsigma$, $\partial v/\partial \varsigma$, $\partial \theta/\partial \varsigma$, and $\partial x/\partial \varsigma$ and using five-point centered differences for $\partial y/\partial \varsigma$, which is identical to $\partial^2 r/\partial \varsigma^2$.

Upon discretization, Eqs. (3)–(5) produce a set of $3N_Z$ algebraic equations containing no time derivatives and converts Eqs. (1), (10), (11), (31), and (35) to a set of $8(N_Z - 1)$ coupled ordinary differential equations containing time derivatives for r, h, y, θ, χ, c_{11}, c_{22}, c_{33}, S_{11}, and S_{33}. The boundary conditions (6)–(9) and (44)–(47) were included in the DAE system as eight algebraic equations.

The resulting DAE system was solved using the double-precision version of the DAE solver DASPK3.0 [Petzold (1983); Maly and Petzold (1996)]. All computations were performed in double-precision FORTRAN using a 2.66 GHz Intel duocore processor-based computer. In coding the dynamic equations, the first grid point was selected at the beginning of the die ($\varsigma=0$). The conditions represented by Eqs. (3)–(8) and (44)–(47) apply at this point. The next N_Z-2 points are interior points. Here, the discretized versions of Eqs. (1), (3)–(5), (10), (11), (31), and (35) were used. At the N_Zth point, all the foregoing equations used for the interior points were applied, except that Eq. (3) was replaced by the discretized version of Eq. (9). Proper scaling of some variables, particularly y in Eq. (3), improved error control and robustness of the computation.

For constant inflation pressure and elongational machine tension F, this strategy of defining and ordering the spatially discretized equations results in a banded Jacobian that greatly speeds up the calculations with DASPK3.0. The inclusion of Eqs. (48) and (49), however, creates a non-banded but still sparse Jacobian that requires a sparse DAE solver for efficient solution.

The calculations started with a low number of grid points, about 101, which were increased until the computed results were unchanged within a minimum of five significant figures of accuracy. For the dependent variables r, h, etc., the minimum grid point allocation, in three zones along the axial direction, that appeared to meet the latter criterion was 81 points uniformly distributed from $\varsigma=0$ to 0.08 (L/R), 155 points uniformly distributed from $\varsigma=0.08$ to 0.30 (L/R), and 85 points uniformly distributed from $\varsigma=0.30$ to 1.00 (L/R), for a total of 321 points. The grid points were spaced more closely near the die to handle the rapid changes that occur from the die to just above the freeze-line.

Although equipped to handle initial conditions that are not consistent, DASPK3.0 performs better when the initial conditions are consistent. To enforce consistency of initial conditions for the DAE system, a preliminary startup condition was often used that evolves into the actual startup condition by smoothly switching parameters over time. Then the simulated time can be reset to zero (by subtracting the time required for the artificial startup) and the real dynamic simulation can begin. Due to hysteresis that sometimes accompanies possible multi-steady states, in general the steady state reached at large time can depend on the intermediate initial condition. No multi-steady-state solutions were discovered in our calculations.

The preliminary startup condition used in the calculations consisted of extruding and attaching the bubble tube to the nip rolls under conditions of uniform (with respect to Z) bubble-tube radius, film thickness, and all other dependent variables. The two operational parameters M_{air} and TUR were then increased from their preliminary to their operational values by using switching functions, which correspond to inflating the bubble and speeding up the nip rolls

$$(M_{air} - M_{air,0})(1 - \exp(-\tau^2/\tau_s^2)) + M_{air,0}, \tag{52}$$

$$(v_L - v_{L,0})(1 - \exp(-\tau^2/\tau_s^2)) + v_{L,0}, \tag{53}$$

where $M_{air,0}$ and $v_{L,0}$ are preliminary values and τ_s is a dimensionless switching time constant usually set as $\tau_s = 10$ to 100. Each switching function has the desirable property that its derivative with respect to time vanishes as τ increases. It was found that DASPK3.0 was more robust if the time derivatives of Eqs. (52) and (53) were used instead of directly using the equations.

Quasi-cylindrical model calculations were made with the steady-state equations presented earlier [Doufas and McHugh (2001); Henrichsen and McHugh (2007)] with some modifications. Two-parameter shooting (on D_1 and $c_{11,0}$) was performed to obtain the desired values of M_{air} and TUR. At a given value of D_1, the value of $c_{11,0}$ resulting in the desired TUR was found by the root-finding method of Brent (1971). The value of D_1 giving the desired value of M_{air} was then found by using the Brent root finding method as well. The imbedded root-finding technique was more robust and accurate than other optimization procedures that were tried. A convenience of the Brent method is that it does not require derivatives. Numerical integration was performed by LSODE [Hindmarsh (1983)] using both the Adams–Moulton and stiff-integration options. Over a typical shooting session, the latter was about 4 times faster as the system of equations gets somewhat stiff at lower values of $c_{11,0}$.

VI. RESULTS AND DISCUSSION

A. Parameter estimation

The thin-shell microstructural (TSMS) model was compared to experimental data obtained at the Clemson University Center for Advanced Engineering Fibers and Films [Cherukupalli (2004); Cherukupalli and Ogale (2004a, 2004b); Cherukupalli *et al.* (2005)]. These data include spatial profiles for bubble-tube radius, film temperature, velocity, and crystallinity. Data points were obtained from plots of Henrichsen (2006) that nicely presented the Clemson data. Table III lists the operating conditions for the first simulation and the values for the physical parameters that correspond to a LLDPE polymer supplied by Dow Chemical (Dowlex). Most of the values in Table III including the operating conditions, crystallization kinetics, material parameters, and heat transfer constants are the same as those used by Henrichsen and McHugh (2007), who fit a QC model to the Clemson data. The exception was that the radiation heat loss term in Eq. (10) was kept separate and not lumped into the convective heat loss term. The TUR was set to 3.8.

The bubble air mass was calculated from the experimental bubble-tube radii and integrating over the bubble volume. The experimental inflation pressure of 840 Pa was then used in Eq. (48) to compute the bubble air mass, although it is a small correction compared to P_{atm}. From $Z = 0$ to the first data point, a straight-line extrapolation was made. Also, an extra volume was added between $Z = L$ and the nip rolls to account for the guide roll region. In this way, the experimental bubble air mass was approximated as 0.0397 g mole. Once set, the bubble air mass is used as a constraint.

The convective heat transfer coefficient was allowed to vary with spatial location according to [Henrichsen and McHugh (2007)]

$$U_h(z) = U_{h,0} + \frac{U_{h,1}}{\left[1 + \exp\left(-\frac{z - z_0}{b}\right)\right]^d}. \tag{54}$$

TABLE III. Values of constants used in simulations.

b	−0.07
C_{pf}	2.427 kJ/kg K
C_{sc}	0.075
d	0.019
D_{crys}	50 K
E_0	1.0
F_{sc}	200
G_{mod}	176 kPa
H_0	0.00025 m
k_{crys}	0.37 s^{-1}
L	0.40 m
M_{air}	0.0397 g mole
N_0	500
R_0	0.0127 m
T_{air}	298 K
T_{max}	368 K
T_0	463 K
$U_{h,0}$	13.0 W/m^2 K
$U_{h,1}$	58.0 W/m^2 K
V_0	0.010625 m/s
α	0.01
α_1	0.688 Pa s
β_1	4388 K
X_f	0.50
ΔH_{crys}	294.1 kJ/kg
ΔP	555.07 Pa
ε	0.96
ρ	920 kg/m^3
σ_{drag}	0.5
ξ, TSMS model	0.90
ξ, MQC model	0.60

The calculations were monitored from startup to near steady state, corresponding to a dimensionless time τ=1000. During this time span, the solutions for r, h, v, θ, χ, y, c_{11}, c_{22}, c_{33}, S_{11}, and S_{33} and the parametric sensitivities evolved significantly before settling down to their steady-state values.

For M_{air}=0.0397 g mole, TUR=3.8, and the conditions in Table III, the computed steady-state bubble-tube radius and film temperature profiles were very close to the experimental profiles [Figs. 2(a) and 3(a)]. In this base case, the computed heat loss due to radiation was only 7.5% of the total, rather than 20% that was expected. For ξ=0.3 suggested by Henrichsen and McHugh (2007), the computed crystallinity profile was lower than experiment, but a good fit was obtained by increasing the enhancement factor ξ to 0.9 [Fig. 3(b)]. As in Henrichsen and McHugh (2007), fitting of the crystallinity points in the lower zone of the bubble tube was favored rather than the crystallinity at Z=L. The calculated inflation pressure of 555.1 Pa for the TSMS model was closer to the experimental value of 840 Pa than the 361 Pa obtained by Henrichsen and McHugh (2007) with their QC model. The TSMS model calculated the machine tension F_z as 1.3142 N. The fact that only a single fitting parameter, ξ, had to be changed demonstrates the capacity of the MQC model to fit data in spite of its lack of curvature terms in the

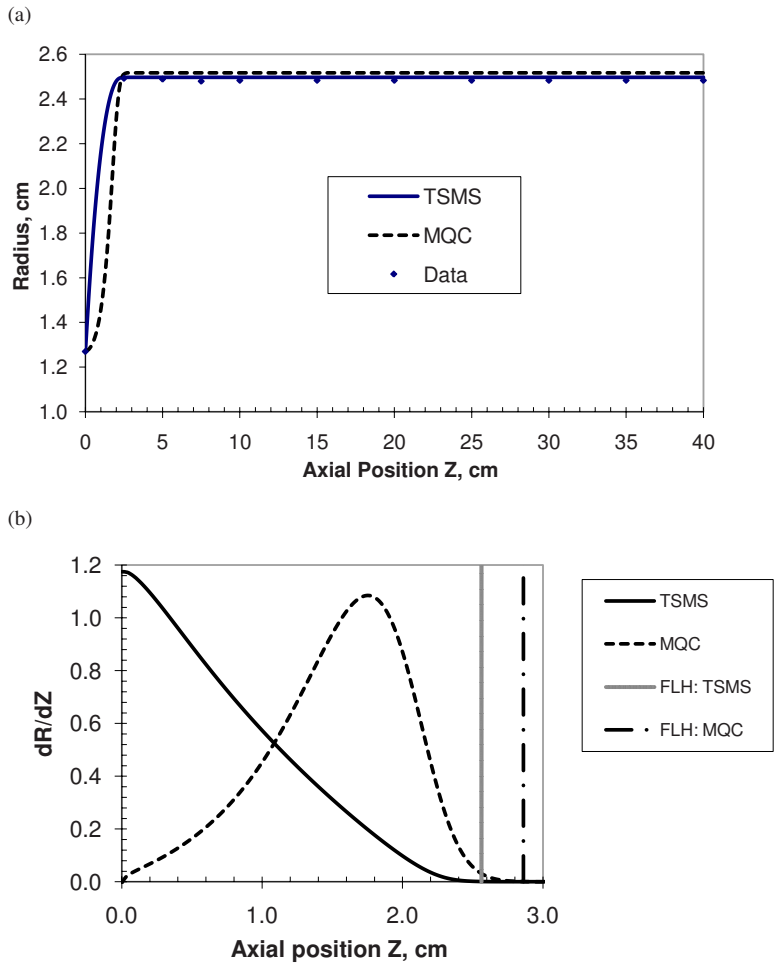

FIG. 2. Comparison of TSMS and MQC models for (a) bubble radius and (b) axial derivative of bubble radius (dR/dZ). None of the profile plots in the manuscript go past Z=40 cm as data were not available and nothing interesting happens beyond that point.

momentum equations. The rapid bubble expansion and low FLHs necessitate plotting only the first zone of the axial domain for clarity [Fig. 2(b)]. The FLH was defined as the axial position above the die where the slope of the bubble-tube radius (dR/dZ) dropped below 10^{-3}. Above this position, the calculated bubble-tube radius and thickness reduction remained constant within five significant figures all the way to Z=L.

For comparison to the TSMS model and the experimental data, profiles for a modified version of the QC model, computed for the same bubble air mass M_{air}, are also shown in Figs. 2(a), 2(b), 3(a), and 3(b). This modified QC (MQC) model uses the same expressions for the velocity gradient tensor $\nabla\mathbf{v}$, which is needed in Eq. (43) for the extra-stress tensor $\boldsymbol{\tau}$, as Henrichsen and McHugh (2007). That is, the secant function ψ in Eqs. (32)–(34) is set to unity. In contrast, our MQC model retains the v/ψ factor in the convection terms in the evolution equations for energy, crystallization, conformation, and orientation, which for the most part resulted in good agreement with the TSMS model and the experimental data. A crystallization-enhancement factor of ξ=0.6 was selected in

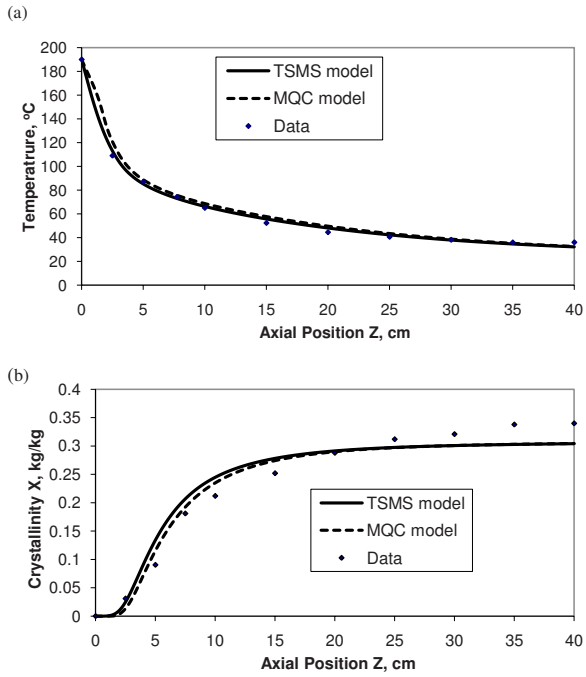

FIG. 3. Comparison of TSMS and MQC models with data for (a) temperature and (b) crystallinity.

the MQC model to fit the crystallinity profile and the results were quantitatively similar to that reported by Henrichsen and McHugh (2007) for the original QC model with $\xi = 0.3$.

As indicated in Figs. 2(a) and 2(b), the most noticeable disagreements between the TSMS and MQC models are bubble shape and the variation of the slope, dR/dZ, of the bubble-tube radius between the die and the FLH. Figure 2(b) shows dR/dZ starting at 1.175 for the TSMS model and monotonically decreasing to essentially zero by the FLH (2.56 cm). In his limited calculations with the TSMS model, Henrichsen (2006) obtained a similar bubble shape, which is called a "pocket bubble" [Cantor (2006)]. In contrast, for the MQC model, dR/dZ starts at -0.004, increases until it reaches a maximum of 1.085 at $Z = 1.76$ cm (an inflection point for the bubble-tube radius), and then declines to near zero at a FLH slightly greater than that of the TSMS model. Between the die and the respective freeze-lines, this gives the bubble tube an initial convex shape for the TSMS model and a concave shape for the MQC model. The larger FLH and the concave shape of the bubble tube diminish the bubble air mass contained in the first 3 cm, so that the MQC model has a slightly higher BUR in the last 47 cm to reach the target bubble air mass of 0.0397 g mole. The divergent behavior of dR/dZ and initial bubble shape between the TSMS and the MQC models occurred for all simulations reported in this paper. In spite of the difference in bubble shape behavior between the die and freeze-line, the BUR and thickness-reduction were comparable. The temperature and crystallinity profiles are quite close together for the two models [Figs. 3(a) and 3(b)].

The corresponding profiles for the total-stress tensor components T_{11} and T_{33} with contributions of the amorphous (T_{11A} and T_{33A}) and semi-crystalline (T_{11sc} and T_{33sc}) phases are shown in Figs. 4(a) and 4(b) for the TSMS model. Both T_{11} and T_{33} plateau very near the freeze-line, while the individual contributions of the two phases continue to

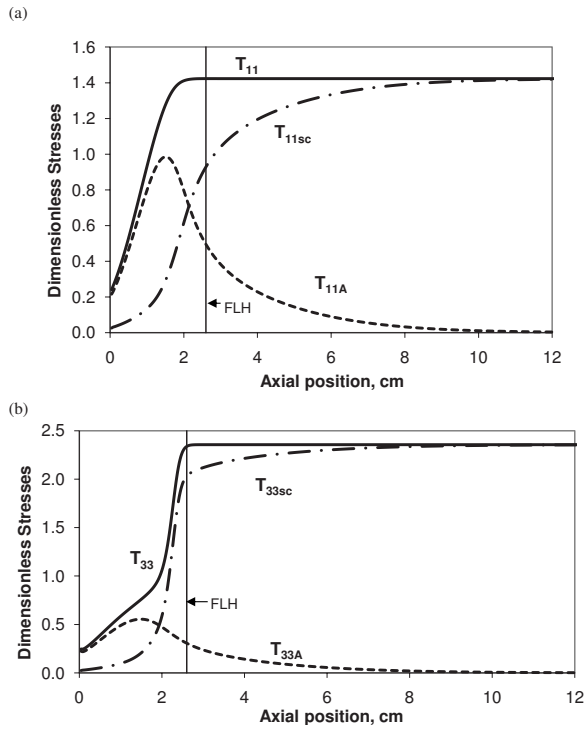

FIG. 4. Spatial profiles for the components of the total stress tensor for the TSMS model: (a) flow direction with amorphous (T_{11A}), semi-crystalline (T_{11sc}), and combined (T_{11}) phases; (b) transverse direction with amorphous (T_{33A}), semi-crystalline (T_{33sc}), and combined (T_{33}) phases. Table III values, $M_{air}=0.0397$ g mole, and TUR=3.8 apply.

vary with position. By Z=10 cm, the stress components T_{11} and T_{33} are nearly completely associated with the semi-crystalline phase. At the freeze-line, the ratios T_{11A}/T_{11} and T_{33A}/T_{33} are important in correlating model predictions with the manufactured film properties of yield stress and elongation at break [Henrichsen (2006); Henrichsen and McHugh (2007)]. The values of T_{11A}/T_{11} and T_{33A}/T_{33} at FLH are 0.358 and 0.136, respectively.

The same total stress variables are plotted in Figs. 5(a) and 5(b) for the MQC model. The plateau values for T_{11} and T_{33} are about 20% lower than those of the TSMS model. The fractional contributions of the amorphous phase to T_{11} and T_{33} show strong agreement between the two models for the axial component, but large differences for the transverse component. For both the TSMS and MQC models, the ratio $T_{11,A}/T_{11}$ is about 0.37 at the respective FLHs (2.56 cm for the TSMS model and 2.86 cm for the MQC model). The ratio $T_{33,A}/T_{33}$, however, is much lower (0.136) at Z=FLH for the TSMS model than the MQC model (0.363). While the T_{11A}/T_{11} values match closely for the TSMS and MQC models, the different computed values of T_{33A}/T_{33} could be significant in predicting mechanical properties of the film in the transverse direction. Thus, this difference was subjected to greater scrutiny.

In Fig. 4(b), T_{33A} for the TSMS model peaks at only 0.553 at Z=1.5 cm and declines thereafter, dropping to 0.315 at the freeze-line. In contrast, for the MQC model T_{33A} peaks at a much larger value of 1.200 at Z=2.0 cm and drops to 0.78 at the freeze-line [Fig. 5(b)]. The persistently low-lying profile of T_{33A} for the TSMS model corresponds to

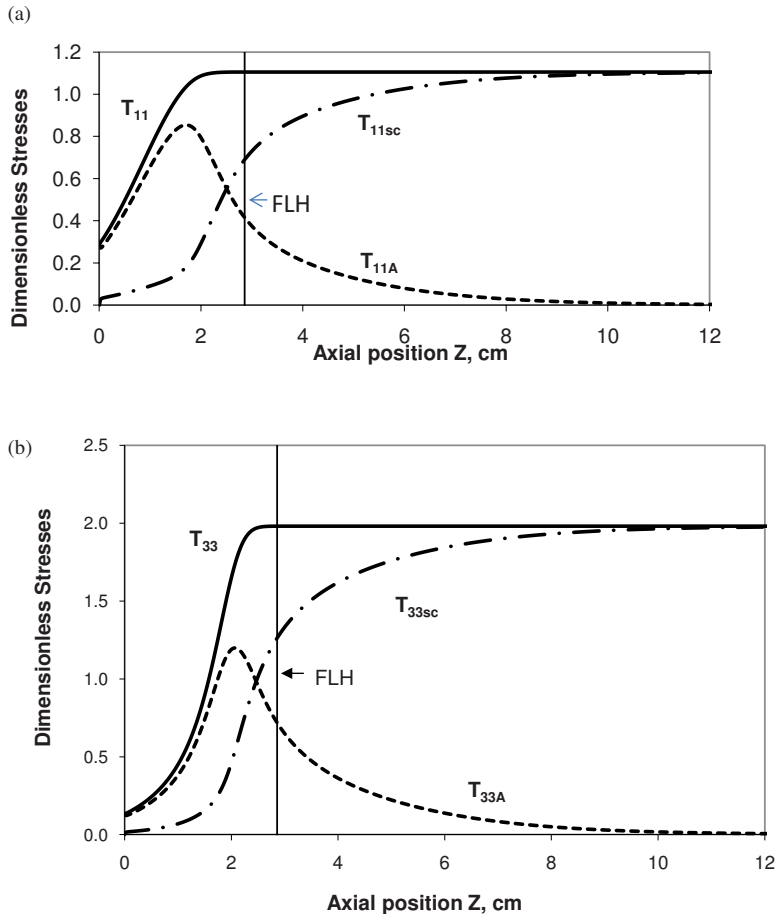

FIG. 5. Spatial profiles for the components of total stress tensor for the MQC model: (a) flow direction with amorphous (T_{11A}), semi-crystalline (T_{11sc}), and combined (T_{11}) phases; (b) transverse direction with amorphous (T_{33A}), semi-crystalline (T_{33sc}), and combined (T_{33}) phases. Table III values, M_{air}=0.0397 g mole, and TUR =3.8 apply.

the lower value of T_{33A}/T_{33} at the freeze-line. The T_{33A} profile closely follows that of the conformation component c_{33} [see Fig. 6(a)] through Eq. (42) and c_{33} depends, in turn, on the transverse component $(\nabla \mathbf{v})_{33}$ of the velocity gradient tensor via Eq. (31). As such, the behavior of $(\nabla \mathbf{v})_{33}$ just above the die [Fig. 6(b)] has an impact on T_{33A} in this zone. The profiles of c_{33} and $(\nabla \mathbf{v})_{33}$ for the MQC model are higher than for the TSMS model in the region before the freeze-line [Figs. 6(a) and 6(b)]. This clarifies the higher value of T_{33A}/T_{33} for the MQC model at its freeze-line and reflects its use of simplified momentum equations.

B. Model sensitivity to operating conditions at constant bubble air mass

Unless air is added or deleted by slitting the bubble, the bubble air mass will remain the same as long as there are no leaks at the nip rolls. For studies at constant bubble air mass, the curves of the BUR versus thickness-reduction at constant inflation pressure presented by many previous investigators were not useful due to the limited variation of the BUR. Here the bubble air mass was held constant at 0.0397 g mole, corresponding to

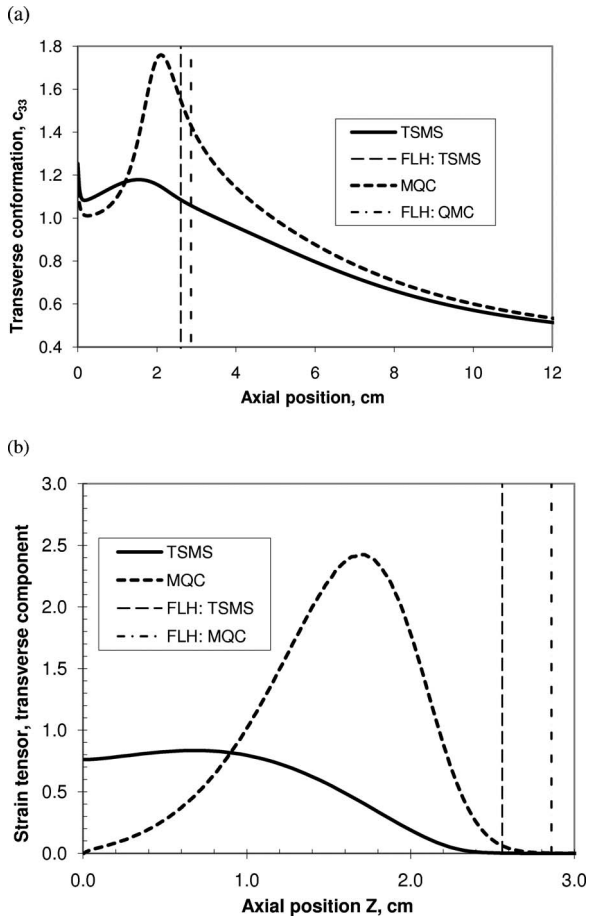

FIG. 6. Comparison of spatial profiles generated by the TSMS and MQC models for the (a) transverse component of dimensionless conformation tensor c_{33} and (b) transverse component of the velocity gradient tensor $(\nabla \mathbf{v})_{33}$. Same parameter values as Figs. 4 and 5.

the fit with the Clemson LLDPE data and the material and operating conditions in Table III, while either TUR or other operating conditions were varied. The purpose was to determine which process variables, other than BUR, were affected and to what extent.

1. Bubble geometry versus TUR at constant bubble air mass

Increasing the TUR can increase thickness-reduction, leading to thinner manufactured films. For the TSMS model at constant M_{air}, the bubble-tube radius profiles just above the die rose slightly with TUR, as did the values of dR/dZ at Z=0, and maintained the convex shape [see Fig. 7(a)]. Temperature profiles were relatively insensitive to TUR [see Fig. 7(b)], while larger changes occurred in the thickness-reduction and crystallinity profiles [Figs. 7(c) and 7(d)].

Due to the limited changes for some variables at constant bubble air mass, the subtle variations are best presented in Table IV. As TUR increases at constant M_{air}, BUR changes only slightly with TUR and these changes track the computed FLH. In order to maintain constant M_{air}, BUR increases as FLH rises. At low TUR, the FLH first increases with TUR due to the shorter residence time allowed for crystallization. As TUR goes

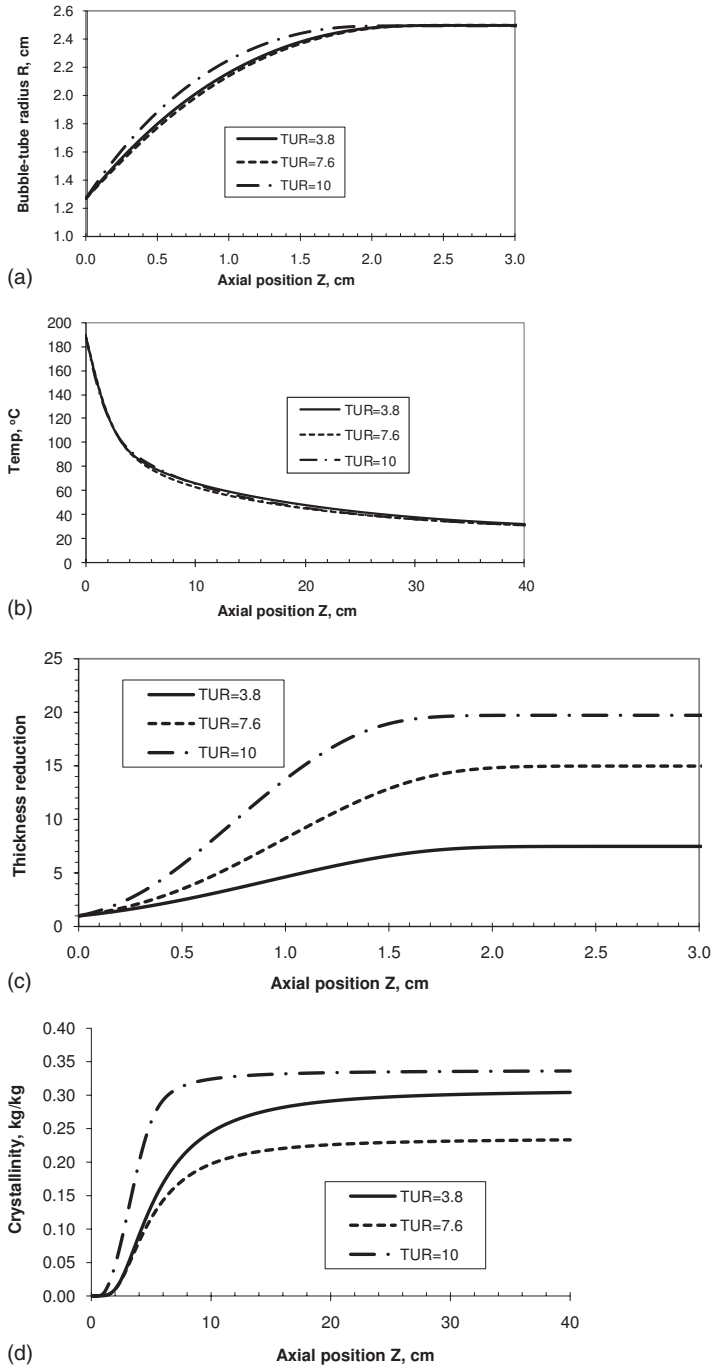

FIG. 7. Effect of TUR on spatial profiles of bubble-tube variables for the TSMS model: (a) bubble-tube radius, (b) temperature, (c) thickness reduction, and (d) crystallinity. Table III conditions apply and M_{air} =0.0397 g mole.

TABLE IV. Bubble geometry versus TUR at M_{air}=0.0397 g mole.

Thin-shell microstructural model						
TUR	FLH	BUR	ThRed	X_{final}	X at FLH	T (°C at FLH)
3.80	2.56	1.9665	7.4782	0.3042	0.027	112
4.50	2.64	1.9668	8.8561	0.2715	0.027	111
6.00	2.68	1.9674	11.8158	0.2343	0.027	110
7.60	2.60	1.9670	14.9715	0.2332	0.027	112
9.00	2.40	1.9656	17.7300	0.2596	0.028	115
10.00	2.20	1.9642	19.7112	0.2918	0.029	119
11.50	1.72	1.9605	22.6003	0.3362	0.031	127
13.50	1.47	1.9584	23.4376	0.3377	0.032	136
MQC model						
TUR	FLH	BUR	ThRed	X_{final}	X at FLH	T (°C at FLH)
3.80	2.86	1.9818	7.5310	0.3045	0.024	114
4.50	2.92	1.9835	8.9258	0.2708	0.023	113
6.00	3.02	1.9859	11.9151	0.2318	0.023	112
7.60	2.96	1.9866	15.0983	0.2270	0.023	114
9.00	2.76	1.9853	17.8678	0.2489	0.023	118
10.00	2.48	1.9821	19.8198	0.2808	0.024	123
10.25	2.36	1.9803	20.2982	0.2915	0.024	125

above 6, however, flow-enhancement of crystallization just above the die causes the FLH to decrease. The crystallinity X_L at the top of the bubble, Z=L, reflects this trend. The crystallinity at the freeze-line is only about 0.03 (column 6 of Table IV) and the temperature has dropped below the melt temperature of 122 °C, except for the highest TUR. The large values of β_1 and F_{sc} result in significant increases in amorphous and semicrystalline relaxation times, enough to essentially lock-in the total stresses only a few centimeters above the die. Thus the bubble-tube radius is constant for the remaining ~46 cm until the film reaches the nip rolls. As expected, thickness-reduction increases with TUR in order to maintain constant polymer mass flow (see columns 1 and 4 of Table IV).

The trends for the MQC model are mostly qualitatively similar to the TSMS model (Table IV). An exception is that there was no solution to the model equations for TUR =11.5, unless $\xi \geq 0.9$, but then the corresponding crystallinity profile would not have matched the data at TUR=3.8. In addition, profiles for the bubble-tube radius show profound early decreases at higher values of TUR before reversing course and rising rapidly to the freeze-line values [see Fig. 8(a)]. Corresponding behavior is exhibited by profiles for the axial derivative of bubble-tube radius [see Fig. 8(b)]. This early decrease in the bubble-tube radius was mentioned by Henrichsen *et al.* (2004), who suggested a proper setting of the parameter C_{sc} in Eq. (27) to suppress it, but this would necessitate resetting C_{sc} for different values of TUR.

2. Stress tensor versus TUR at constant bubble air mass

For the TSMS model at constant M_{air}, inflation pressure ΔP and machine tension F_z both increase with TUR (Table V). The plateau values of the total stress tensor compo-

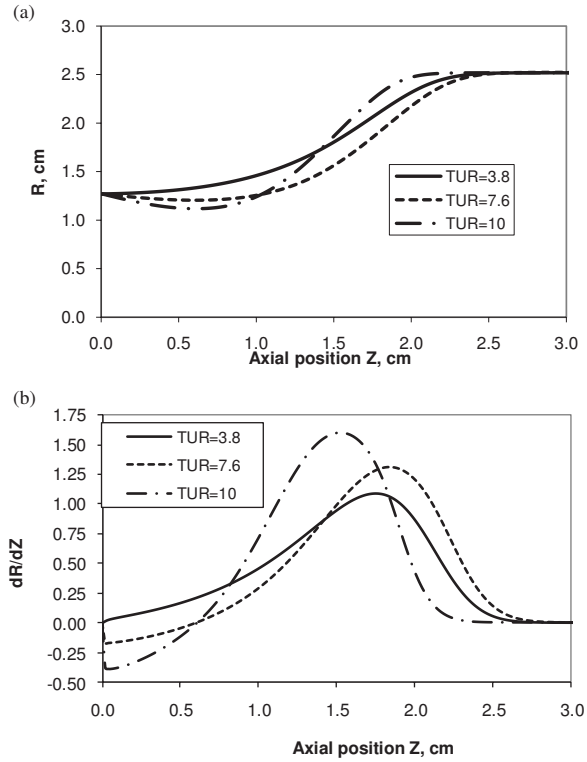

FIG. 8. Effect of TUR on spatial profiles of (a) the bubble-tube radius and (b) its axial derivative dR/dZ for the MQC model. Table III conditions apply and M_{air}=0.0397 g mole.

nents T_{11} and T_{33}, which are practically reached at Z=FLH, both increase with TUR. Their overall spatial profiles are elevated with increasing TUR [Figs. 9(a) and 9(b)]. The fractional contributions of the amorphous phase to the total-stress tensor components at Z=FLH show trends in Table V; the ratio in the flow direction increases with TUR and the ratio in the transverse direction declines. The dimensionless stored free energy profile also shows an increase with TUR [see Fig. 9(c)], which enhances the crystallization kinetics. As mentioned above, for the higher TUR values, the increase in the crystallization rate overcomes the lower residence time of the film in the zone of maximum crystallization. This behavior at higher TUR was observed experimentally [Cherukupalli and Ogale (2004b)].

The MQC model shows the same trends for stress variables as the TSMC model, as indicated at the bottom of Table V, except for the fraction of the amorphous contribution to the total-stress tensor in the transverse direction at Z=FLH. As pointed out earlier, it is much larger than for the TSMC model. Also, the fraction of the amorphous contribution rises with TUR, whereas T_{33A}/T_{33} decreases with TUR for the TSMC model. Thus, the two models predict different trends in the yield stress and elongation at break for the transverse direction [Henrichsen and McHugh (2007)].

3. Effect of convective heat transfer at constant M_{air}

To determine the effect that convective heat transfer might have on operating variables at constant M_{air}, the right side of the expression for U_h in Eq. (54), which corresponds to

TABLE V. Stress variables versus TUR at M_{air}=0.0397 g mole.

Thin-shell microstructural model						
TUR	ΔP (Pa)	F_z (N)	T_{11} at FLH	T_{33} at FLH	T_{11A}/T_{11} at FLH	T_{33A}/T_{33} at FLH
3.80	555.1	1.3142	1.424	2.323	0.358	0.136
4.50	564.5	1.4083	1.806	2.799	0.401	0.142
6.00	590.7	1.5822	2.706	3.892	0.485	0.145
7.60	645.9	1.7675	3.831	5.389	0.555	0.132
9.00	743.7	1.9645	5.046	7.302	0.611	0.114
10.00	875.3	2.1537	6.155	9.563	0.644	0.095
11.50	1361.4	2.6301	8.633	17.039	0.684	0.061
13.50	2093.8	3.4225	11.661	27.346	0.698	0.042
MQC model						
TUR	ΔP (Pa)	F_z (N)	T_{11} at FLH	T_{33} at FLH	T_{11A}/T_{11} at FLH	T_{33A}/T_{33} at FLH
3.80	459.7	1.0209	1.106	1.980	0.375	0.363
4.50	468.6	1.0922	1.400	2.394	0.425	0.405
6.00	485.5	1.2277	2.098	3.316	0.497	0.461
7.60	507.4	1.3866	3.001	4.393	0.569	0.514
9.00	538.8	1.5948	4.088	5.517	0.627	0.560
10.00	584.6	1.8991	5.409	6.629	0.667	0.591
10.25	608.8	2.0683	6.039	7.064	0.674	0.596

the high cooling condition of the experimental operation, was multiplied by 0.90, 0.95, 1.05, and 1.10. Perturbations of this magnitude could be achieved by decreasing or increasing the flow through the air ring.

The results for bubble geometry are too subtle to see in profile plots, so they are reported in Table VI. The FLH decreases with increased U_h and BUR tracks FLH. Thickness-reduction declines as BUR declines to conserve polymer mass flow. The crystallinity at the top of the bubble tube, X_L, decreases with increased U_h. This is caused by the Gaussian dependence of crystallization rate on temperature and that a large value of U_h rapidly dropped the film temperature below the optimum value T_{max}. The MQC model follows the same trend.

For the TSMS model, the inflation pressure and machine tension increase with increased U_h as the bubble-tube relaxation times increase with lower temperature (see Table VII). This is reflected in the components of the total stress tensor. The amorphous fraction of the total-stress tensor T_{11A}/T_{11} in the flow direction at Z=FLH increases as convective cooling increases. On the other hand, for the TSMS model, the same fraction in the transverse direction, T_{33A}/T_{33}, decreases with increased U_h and is noticeably smaller than T_{11A}/T_{11}.

The qualitative trends for machine tension, inflation pressure, and the total stress tensor are similar between the MQC model, but not to the same extent. Also, T_{11A}/T_{11} and T_{33A}/T_{33} at Z=FLH both increase with convective cooling and the latter is closer to the former in value. In summary, the TSMS and MQC models give different sensitivities and in one case a different trend for the effect of changes in convective cooling U_h on locked-in stresses and the corresponding prediction of film properties.

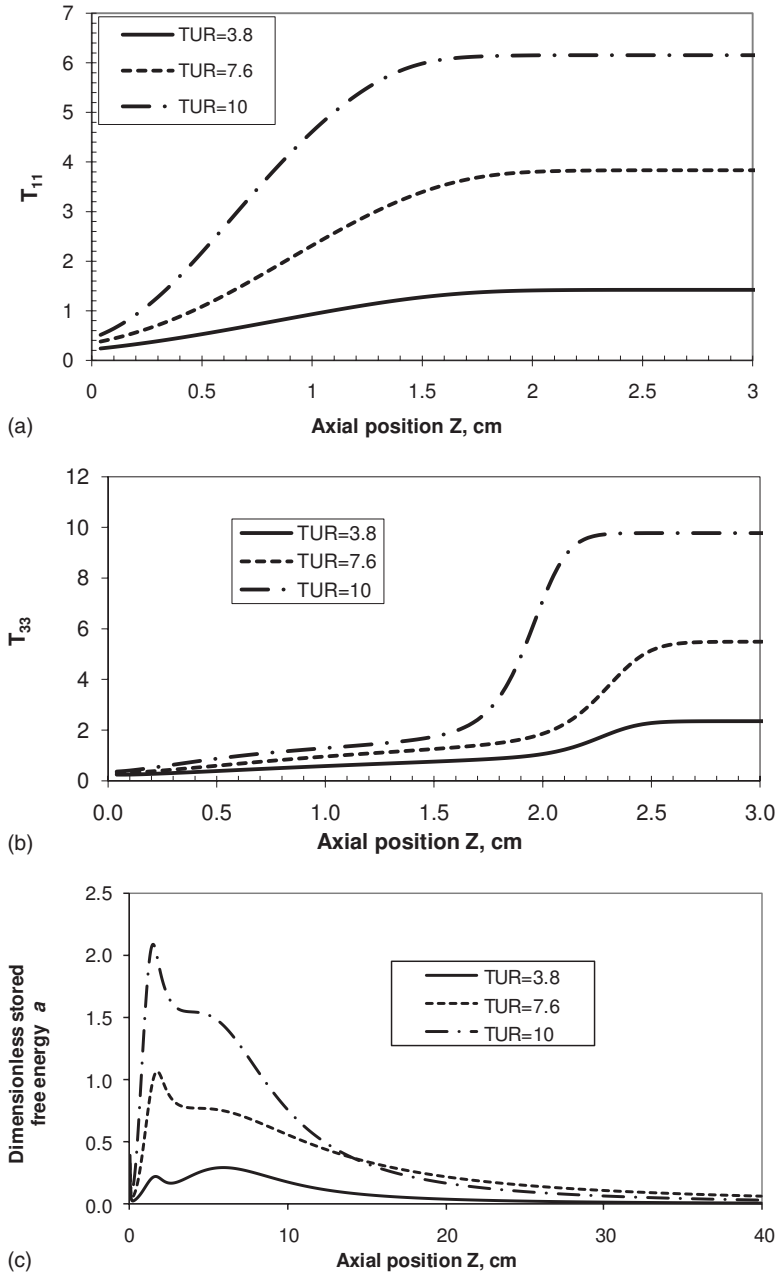

FIG. 9. Effect of TUR on the spatial profiles of stress variables for the TSMS model: (a) total stress in the flow direction, T_{11}; (b) total stress in the transverse direction, T_{33}; (c) stored free energy a. Table III conditions apply and M_{air}=0.0397 g mole.

4. Effect of extrusion temperature at constant M_{air}

Intuitively, it might seem that small changes in the extrusion temperature might have a noticeable effect of blown film operation. To examine this premise, T_0 was set to levels slightly above and below 463 K and the other values in Table III remained the same. For parameter and variable normalization, the reference temperature T_{ref} was kept at 463 K.

TABLE VI. Bubble geometry versus heat transfer coefficient U_h at TUR=3.8, M_{air}=0.0397 g mole.

Thin-shell microstructural model						
U_h factor	FLH (cm)	BUR	ThRed	X_L (kg/kg)	X at FLH (kg/kg)	Temp. (°C at FLH)
0.90	2.80	1.9685	7.4843	0.3462	0.026	113
0.95	2.68	1.9674	7.4802	0.3252	0.027	113
1.00	2.56	1.9665	7.4782	0.3042	0.027	112
1.05	2.44	1.9656	7.4763	0.2839	0.027	112
1.10	2.32	1.9647	7.4735	0.2649	0.027	111
MQC model						
U_h factor	FLH (cm)	BUR	ThRed	X_L (kg/kg)	X at FLH (kg/kg)	Temp. (°C at FLH)
0.90	3.16	1.9905	7.5640	0.3477	0.026	115
0.95	3.00	1.9837	7.5380	0.3261	0.024	114
1.00	2.86	1.9818	7.5310	0.3045	0.024	114
1.05	2.72	1.9802	7.5246	0.2837	0.024	113
1.10	2.60	1.9802	7.5246	0.2644	0.024	113

The effects of T_0 on bubble geometry, crystallization, and stress variables are reported in Tables VIII and IX for both the TSMS and MQC models. The TSMS model shows that modest changes in bubble geometry occur with varying T_0 that mainly track FLH, which increases with increased T_0. The stress variables are much more sensitive to extrusion temperature, with significant decreases in the inflation pressure and machine tension with

TABLE VII. Stress variables versus heat transfer coefficient U_h at TUR=3.8, M_{air}=0.0397 g mole.

Thin-shell microstructural model						
U_h factor	ΔP (Pa)	F_z (N)	T_{11} at FLH	T_{33} at FLH	T_{11A}/T_{11} at FLH	T_{33A}/T_{33} at FLH
0.90	476.8	1.2207	1.322	1.993	0.341	0.142
0.95	514.7	1.2676	1.373	2.155	0.348	0.138
1.00	555.1	1.3142	1.423	2.324	0.358	0.136
1.05	597.9	1.3606	1.474	2.498	0.369	0.134
1.10	643.3	1.4064	1.524	2.678	0.381	0.132
MQC model						
U_h factor	ΔP (Pa)	F_z (N)	T_{11} at FLH	T_{33} at FLH	T_{11A}/T_{11} at FLH	T_{33A}/T_{33} at FLH
0.90	422.0	0.9219	0.998	1.825	0.352	0.341
0.95	440.6	0.9704	1.050	1.901	0.365	0.353
1.00	459.7	1.0209	1.105	1.980	0.375	0.363
1.05	479.3	1.0737	1.162	2.061	0.387	0.374
1.10	499.6	1.1294	1.222	2.145	0.395	0.381

TABLE VIII. Bubble geometry versus extrusion temperature T_0 at TUR=3.8, M_{air}=0.0397 g mole.

Thin-shell microstructural model

T_0	FLH (cm)	BUR	ThRed	X_L (kg/kg)	X at FLH (kg/kg)	Temp. (°C at FLH)
458	2.38	1.9650	7.4688	0.2986	0.027	112
461	2.48	1.9658	7.4761	0.3018	0.027	112
463	2.56	1.9665	7.4782	0.3042	0.027	112
465	2.60	1.9670	7.4794	0.3066	0.026	112
468	2.68	1.9678	7.4822	0.3101	0.026	112

MQC model

T_0	FLH (cm)	BUR	ThRed	X_L (kg/kg)	X at FLH (kg/kg)	Temp. (°C at FLH)
458	2.64	1.9790	7.5204	0.2976	0.024	114
461	2.78	1.9809	7.5269	0.3018	0.024	114
463	2.86	1.9818	7.5310	0.3045	0.024	114
465	2.94	1.9829	7.5350	0.3057	0.024	113
468	3.06	1.9844	7.5409	0.3114	0.024	113

increased T_0 for the same bubble air mass. The components of the total stress tensor at the FLH also decline with increased T_0, while the ratios T_{11A}/T_{11} and T_{33A}/T_{33} show a slight increase.

TABLE IX. Stress variables versus extrusion temperature T_0 at TUR=3.8, M_{air}=0.0397 g mole.

Thin-shell microstructural model

T_0	ΔP (Pa)	F_z (N)	T_{11} at FLH	T_{33} at FLH	T_{11A}/T_{11} at FLH	T_{33A}/T_{33} at FLH
458	671.0	1.4908	1.614	2.801	0.349	0.126
461	597.2	1.3804	1.495	2.526	0.357	0.131
463	555.1	1.3142	1.423	2.323	0.358	0.136
465	517.6	1.2529	1.357	2.153	0.368	0.145
468	468.9	1.1693	1.266	1.942	0.376	0.155

MQC model

T_0	ΔP (Pa)	F_z (N)	T_{11} at FLH	T_{33} at FLH	T_{11A}/T_{11} at FLH	T_{33A}/T_{33} at FLH
458	524.7	1.1999	1.299	2.254	0.371	0.355
461	483.8	1.0861	1.176	2.082	0.372	0.358
463	459.7	1.0209	1.105	1.980	0.375	0.363
465	437.6	0.9625	1.042	1.887	0.377	0.366
468	407.8	0.8853	0.958	1.761	0.379	0.369

TABLE X. Bubble geometry versus bubble air mass M_{air} and TUR.

Thin-shell microstructural model							
M_{air} (g mole)	TUR	FLH (cm)	BUR	ThRed	X_{final} (kg/kg)	X at FLH (kg/kg)	T (°C at FLH)
0.0397	3.8	2.56	1.9665	7.4725	0.3042	0.027	112
0.0438	3.8	2.36	2.0632	7.8401	0.2773	0.027	111
0.0469	3.8	2.20	2.1340	8.1093	0.2587	0.028	111
0.0438	4.5	2.43	2.0640	9.2914	0.2476	0.027	110
0.0469	4.5	2.26	2.1347	9.6105	0.2312	0.027	110
MQC model							
M_{air} (g mole)	TUR	FLH (cm)	BUR	ThRed	X_{final} (kg/kg)	X at FLH (kg/kg)	T (°C at FLH)
0.0397	3.8	2.86	1.9818	7.5310	0.3045	0.0240	114
0.0438	3.8	2.80	2.0797	7.9027	0.2796	0.0295	111
0.0469	3.8	2.60	2.1510	8.1738	0.2631	0.0287	111
0.0438	4.5	2.78	2.0810	9.3645	0.2500	0.0260	112
0.0469	4.5				No solution		

C. Effect of increasing bubble air mass on computed process variables

Increasing the bubble air mass is expected to increase the BUR and the thickness-reduction which, in many cases, are desirable goals. As the appropriate expression for convective heat transfer has been shown to be sensitive to bubble size [Henrichsen (2006)], the bubble air mass was restricted to 0.0469 g mole or below so that the values of the constants for Eq. (54) in Table III could still be used. Bubble geometry for the TSMS and MQC models follows the expected trend (see Tables X and XI for two values of the TUR). At a constant TUR, both the BUR and thickness-reduction increase with bubble air mass. The FLH declines with increased bubble air mass, primarily due to increased cooling and stress-enhanced crystallization. Due to the high value of F_{sc}, only a small crystallinity is necessary to stiffen the flowing film and keep the bubble-tube radius from growing further. This acute effect of crystallinity on the system stiffness agrees with past studies [Doufas and McHugh (2001); Henrichsen *et al.* (2004); Henrichsen and McHugh (2007)]. The TS and MQC models have the same qualitative behavior. No solution could be found for the MQC model when M_{air}=0.0469 g mole and TUR =4.5. Plotting a family of BUR versus TUR curves, at constant inflation pressure, revealed there was no solution at these conditions.

The calculated inflation pressure and machine tension both increase as M_{air} increases at constant TUR. This trend also holds for the components of the total-stress tensor at the FLH, which are virtually the same as the corresponding values at Z=L. In the flow direction, the ratio of the amorphous phase to the total-stress tensor increases with increased M_{air} for a constant TUR. For the TSMS model, the equivalent ratio in the transverse direction, T_{33A}/T_{33}, decreases with increased M_{air}. For the MQC model, both T_{11A}/T_{11} and T_{33A}/T_{33} increase with increased M_{air} at constant TUR.

D. Sensitivity of models to fitting parameters

1. Semi-crystalline relaxation time factor F_{sc}

An important parameter for determining the semi-crystalline relaxation time is F_{sc} in Eq. (27). In fitting their QC model to the Clemson data, Henrichsen and McHugh (2007)

TABLE XI. Stress variables versus bubble air mass M_{air} and TUR.

Thin-shell microstructural model							
M_{air} (g mole)	TUR	ΔP (Pa)	F_z (N)	T_{11} at FLH	T_{33} at FLH	T_{11A}/T_{11} at FLH	T_{33A}/T_{33} at FLH
0.0397	3.8	555.1	1.3142	1.424	2.323	0.358	0.136
0.0438	3.8	604.8	1.3809	1.496	2.786	0.365	0.123
0.0469	3.8	646.8	1.4284	1.546	3.187	0.370	0.114
0.0438	4.5	615.6	1.4775	1.892	3.357	0.402	0.124
0.0469	4.5	659.7	1.5273	1.958	3.835	0.418	0.119
MQC model							
M_{air} (g mole)	TUR	ΔP (Pa)	F_z (N)	T_{11} at FLH	T_{33} at FLH	T_{11A}/T_{11} at FLH	T_{33A}/T_{33} at FLH
0.0397	3.8	459.7	1.0209	1.105	1.980	0.375	0.363
0.0438	3.8	487.2	1.0912	1.181	2.311	0.347	0.341
0.0469	3.8	514.3	1.1613	1.257	2.610	0.360	0.358
0.0438	4.5	497.0	1.1711	1.501	2.796	0.414	0.401
0.0469	4.5				No solution		

found that a large value of F_{sc} was required to produce a sudden rise in the bubble-tube radius. To determine system sensitivity to F_{sc} in this high range, F_{sc} was set to 100, 200 (its base value in Table III), and 300. The TUR was set at 3.8 and M_{air} was set to 0.0397 g mole. For both TSMS and MQC models, the FLH, BUR, thickness-reduction, and crystallinity at Z=L decreased as F_{sc} increased (see Table XII). Inflation pressure, machine tension, and total stress at the freeze-line increased for both models (Table XIII), which was expected as the film stiffens with increasing F_{sc}. The contribution of the

TABLE XII. Bubble geometry versus semi-crystalline relaxation time factor F_{sc} at TUR=3.8 and M_{air} =0.0397 g mole.

Thin-shell microstructural model						
F_{sc}	FLH (cm)	BUR	ThRed	X_L (kg/kg)	X at FLH (kg/kg)	Temp. (°C at FLH)
100	3.20	1.9711	7.4935	0.3120	0.048	104
200	2.56	1.9665	7.4782	0.3042	0.027	112
300	2.24	1.9641	7.4708	0.2998	0.019	117
MQC model						
F_{sc}	FLH (cm)	BUR	ThRed	X_L (kg/kg)	X at FLH (kg/kg)	Temp. (°C at FLH)
100	3.60	1.9885	7.55620	0.3136	0.046	105
200	2.86	1.9818	7.5310	0.3045	0.024	114
300	2.52	1.9783	7.5177	0.2996	0.017	118

TABLE XIII. Stress variables versus semi-crystalline relaxation time factor F_{sc} at TUR=3.8 and M_{air} =0.0397 g mole.

Thin-shell microstructural model						
F_{sc}	ΔP (Pa)	F_z (N)	T_{11} at FLH	T_{33} at FLH	T_{11A}/T_{11} at FLH	T_{33A}/T_{33} at FLH
100	443.9	1.2312	1.333	1.859	0.356	0.170
200	555.1	1.3142	1.423	2.323	0.358	0.136
300	640.7	1.3669	1.481	2.636	0.371	0.125
MQC model						
F_{sc}	ΔP (Pa)	F_z (N)	T_{11} at FLH	T_{33} at FLH	T_{11A}/T_{11} at FLH	T_{33A}/T_{33} at FLH
100	417.3	0.9166	0.987	1.810	0.360	0.347
200	459.7	1.0209	1.105	1.980	0.375	0.363
300	490.8	1.1033	1.194	2.107	0.375	0.363

amorphous phase to the axial component of the total stress tensor increased slightly for both models with increased F_{sc}; the equivalent contribution to T_{33} moved in opposite directions for the TSMS and MQC models.

2. Flow-enhanced crystallization factor ξ

Another important parameter in fitting the QC model to the Clemson data was the factor ξ for flow-enhanced crystallization [Henrichsen and McHugh (2007)]. At constant bubble air mass (0.0397 g mole) and TUR (3.8), Tables XIV and XV show the effect of changing ξ upon bubble geometry and stress variables. For the TSMS and MQC models,

TABLE XIV. Bubble geometry versus crystallization enhancement factor ξ at TUR=3.8 and M_{air} =0.0397 g mole.

Thin-shell microstructural model						
ξ	FLH (cm)	BUR	ThRed	X_L (kg/kg)	X at FLH (kg/kg)	Temp. (°C at FLH)
0.15	2.64	1.9673	7.4805	0.2630	0.026	111
0.3	2.63	1.9671	7.4762	0.2710	0.026	111
0.6	2.59	1.9669	7.4759	0.2873	0.026	112
0.9	2.56	1.9665	7.4782	0.3042	0.027	112
1.2	2.51	1.9660	7.4717	0.3220	0.027	113
MQC model						
ξ	FLH (cm)	BUR	ThRed	X_L (kg/kg)	X at FLH (kg/kg)	Temp. (°C at FLH)
0.15	2.96	1.9830	7.5353	0.2799	0.024	112
0.30	2.94	1.9826	7.5340	0.2880	0.024	112
0.60	2.86	1.9818	7.5310	0.3045	0.024	114
0.90	2.78	1.9811	7.5281	0.3211	0.024	115

TABLE XV. Stress variables versus crystallization enhancement factor ξ at TUR=3.8 and M_{air} =0.0397 g mole.

Thin-shell microstructural model

ξ	ΔP (Pa)	F_z (N)	T_{11} at FLH	T_{33} at FLH	T_{11A}/T_{11} at FLH	T_{33A}/T_{33} at FLH
0.15	530.2	1.2979	1.405	2.204	0.369	0.147
0.3	534.8	1.3009	1.408	2.229	0.365	0.144
0.6	544.6	1.3075	1.415	2.271	0.363	0.141
0.9	555.1	1.3142	1.423	2.323	0.358	0.136
1.2	565.6	1.3209	1.430	2.359	0.359	0.134

MQC model

ξ	ΔP (Pa)	F_z (N)	T_{11} at FLH	T_{33} at FLH	T_{11A}/T_{11} at FLH	T_{33A}/T_{33} at FLH
0.15	451.4	0.9993	1.082	1.947	0.380	0.367
0.30	454.0	1.0061	1.089	1.957	0.375	0.363
0.60	459.7	1.0209	1.105	1.980	0.375	0.363
0.90	465.9	1.0373	1.123	2.006	0.375	0.363

FLH, BUR, and thickness-reduction decrease as ξ increases (see Table XIV). Crystallinity at the FLH is small and the corresponding temperature is below the melting point. Crystallinity at the top of the bubble (Z=L) increases with ξ, as expected. With increased ξ, the inflation pressure, machine tension, and both components of the total stress tensor at Z=FLH increase and T_{11A}/T_{11} and T_{33A}/T_{33} decrease slightly. Most trends are the same for both the TSMS and MQC models, but the amorphous phase ratios T_{11A}/T_{11} and T_{33A}/T_{33} plateau when $\xi \geq 0.3$ for the latter.

3. Bulk shear modulus G_{mod}

The bulk shear modulus G_{mod} influences the value of the relaxation times through Eqs. (24) and (25). To examine the effect G_{mod} has on results for TS/MS and MQC models, values of G_{mod} above and below the base value of 176 kPa were tried. Reasonably large variations in G_{mod} had modest effects on bubble geometry (Table XVI). For both models, FLH increases with G_{mod}, but only slight changes in BUR and thickness reduction occur. The end crystallinity X_L changes more, declining as G_{mod} increases. Changes in the stress variables are more noticeable, with inflation pressure increasing with increased G_{mod} for both models, but the machine tension increasing for the TSMS model while decreasing for the MQC model (Table XVII). The axial and transverse components of total stress and the fractional contributions by the amorphous phase to the total stress decline with increased G_{mod} for both models.

E. Sensitivity to boundary conditions

1. Upper boundary condition for TSMS model

For the computations reported above with the TSMS model, the upper boundary condition set at Z=L was Eq. (9), which is the minimum-order reduction boundary condition. This boundary condition avoids the non-physical kinks in the computed

TABLE XVI. Bubble geometry versus bulk shear modulus G_{mod} at TUR=3.8 and M_{air}=0.0397 g mole.

Thin-shell microstructural model						
G_{mod} (Pa)	FLH (cm)	BUR	ThRed	X_L (kg/kg)	X at FLH (kg/kg)	Temp. (°C at FLH)
130000	2.48	1.966	7.476	0.328	0.027	113
176000	2.56	1.967	7.478	0.304	0.027	112
225000	2.60	1.967	7.476	0.292	0.027	111
MQC model						
G_{mod} (Pa)	FLH (cm)	BUR	ThRed	X_L (kg/kg)	X at FLH (kg/kg)	Temp. (°C at FLH)
130000	2.74	1.981	7.526	0.322	0.024	115
176000	2.86	1.982	7.531	0.305	0.024	114
225000	2.96	1.983	7.534	0.296	0.024	113

bubble-tube radius profiles that can result when some other boundary conditions are used. Results of applying other boundary conditions for the same conditions as the above simulations are discussed here.

First consider the zero-order reduction boundary condition, which is having the actual momentum equation, Eq. (5), holds at Z=L. In essence, this corresponds to neglecting the upper boundary condition and solving the problem like a hyperbolic system. When this was done, all computed results were the same within the numerical error produced by using fourth-order finite-difference approximations to spatial derivatives, about seven significant figures of accuracy. The success of this approach for the simulated conditions is probably due to the high degree of crystallization and its effect on system stiffness. The computational time using this alternative boundary condition is the same as that of using Eq. (5), so the latter should still be used especially for cases that do not involve such a profound effect of crystallization.

TABLE XVII. Stress variables versus bulk shear modulus G_{mod} at TUR=3.8 and M_{air}=0.0397 g mole.

Thin-shell microstructural model						
G_{mod} (kPa)	ΔP (Pa)	F_z (N)	T_{11} at FLH	T_{33} at FLH	T_{11A}/T_{11} at FLH	T_{33A}/T_{33} at FLH
130	550.5	1.287	1.887	3.120	0.436	0.148
176	555.1	1.314	1.423	2.323	0.358	0.136
225	563.9	1.339	1.134	1.844	0.295	0.121
MQC model						
G_{mod} (kPa)	ΔP (Pa)	F_z (N)	T_{11} at FLH	T_{33} at FLH	T_{11A}/T_{11} at FLH	T_{33A}/T_{33} at FLH
130	447.6	1.041	1.525	2.549	0.454	0.432
176	459.7	1.021	1.105	1.980	0.375	0.363
225	477.4	1.019	0.863	1.610	0.309	0.300

Calculations were also performed where the upper position L of the spatial boundary was lowered from L=50 to 40, 30, 20, or 10 cm. The geometric and stress tensor profiles matched closely (within five significant figures) over their overlapping ranges. This shows that the system is so frozen-in at the freeze-line that the position of the upper boundary has little effect, as long as it is a sufficient distance above the freeze-line.

Surprisingly, if the boundary condition

$$\frac{\partial \mathrm{r}}{\partial \tau} + \frac{\mathrm{v}}{\psi}\frac{\partial \mathrm{r}}{\partial \mathrm{s}} = 0, \tag{55}$$

advocated by many previous investigators [Cain and Denn (1988); Hyun *et al.* (2004); Shin *et al.* (2007)], was used, the computational time to reach steady state increased by a factor of 4. Also, the last several grid points in the spatial domain exhibited erratic values for the bubble-tube radius, even though the bubble-tube radius was frozen-in far below Z=L. Thus, it is apparent that the minimum-order or zero-order reduction boundary conditions should be used, preferably the former as it is mathematically tenable.

2. Partitioning of momentum equations at the die

All of the computations performed above for the TSMS model utilized Eqs. (44)–(47), which involve partitioning of the momentum equations into contributions from the amorphous and semi-crystalline phases. This approach was explored by Shrikhande *et al.* (2006) and Henrichsen and McHugh (2007). If these equations were not used and the components of the orientation tensor **S** were simply set to zero at Z=0, the difference in results for the base case was slight, but grew somewhat for the more stressful cases. The small amount of semi-crystalline stress at Z=0, which may be physically inconsistent, in Figs. 4 and 5 also disappeared. Regardless of its appropriateness, however, the partitioned-momentum condition causes no computational inconvenience in our numerical approach.

F. Computer resource requirement

The dynamic TSMS model is a DAE system with several thousand equations. Using DASPK3.0, which handles stiff equations, calculations required 90 CPU s with the Intel 266 MHz processor when the inflation pressure and machine tension was held constant. For constant bubble air mass and TUR, more time is required due to the non-banded, but still sparse, system Jacobian. Using the full dense Jacobian option in DASPK3.0 required 60–150 CPU min, but our experience with DAE solvers for sparse systems indicates the computation time can be as low as 120 CPU s. Solution of the steady-state equations directly might save even more time, but continuation methods are often needed due to the possibility of multi-steady states. Solution of the dynamic equations can also handle difficult boundary conditions, such as Eqs. (44)–(47), by the use of preliminary startup conditions.

At steady-state, the QC model is a small differential-algebraic system of equations that can be converted into an initial-value system of ordinary differential equations. A typical shooting session in which the targets are set for the bubble air mass and TUR required about 100 CPU s using our imbedded root-finding method. This could be speeded up with a good optimization scheme. The rapid solution of the QC model with readily available numerical methods makes it useful for preliminary estimation of material parameters from experimental data.

VII. CONCLUSIONS

This paper demonstrates the practicality of combining the thin-shell model for blown film extrusion with the microstructural constitutive relation (the TSMS model). The location of the freeze-line was automatically determined by the substantial effect of crystallization on the relaxation time of the semi-crystalline phase. Flow-enhanced crystallization augments this locking-in effect. When compared to a MQC model, which neglects the effect of axial curvature in the momentum equations but not in the conservation equations for temperature, crystallinity, conformation, and orientation equations, there is mostly strong agreement with respect to data fitting and operational predictions of bubble geometry, FLH, temperature, crystallization, and stress variables. The effects of TUR, convective heat transfer, extrusion temperature, and some key material parameters all show similar qualitative trends for the TSMS and MQC models. Most sensitivity studies with the two models showed good qualitative agreement.

For some variables, there is also good quantitative agreement, especially for the locked-in stresses in the flow direction. There are some deviations in the bubble shape between the die and the freeze-line, which is only a short distance due to the early lock-in by crystallization. This seemingly subtle difference leads to noticeable differences in the computed amorphous-phase contributions to the total stress tensor in the transverse direction at the freeze-line. This could lead to erroneous predictions of mechanical properties for the film in the transverse direction, indicating the simplified momentum equations used by the MQC model should not be used for prediction of those variables. Also, at higher values of the bubble air mass, the MQC model sometimes had no steady-state solution when the TSMS model did, indicating that the MQC model should be used with care under those conditions.

On the other hand, the ease of implementation of the steady-state MQC model makes it suitable for preliminary fitting of experimental data, estimating material and transport parameters, and scoping operating conditions. Using the MQC model in the early stages of blown film analysis and the more rigorous TSMS model in the later stages might be an effective strategy.

The upper boundary condition, at Z=L, needed to be of the minimum-order reduction or zero-order reduction form to avoid anomalies in computed bubble-tube radius and its axial derivative for the conditions treated in this paper. The upper boundary at L could be lowered to about twice the FLH without significantly affecting any of the computed profiles. The TSMS model naturally locates the freeze-line as long as L is a moderate distance above where it occurs.

Partitioning the momentum equations into contributions by the amorphous and semicrystalline phases at the die, rather than setting the components of the orientation tensor to zero, is not only necessary on physical grounds but also for accurate numerical results in high stress conditions.

References

Ashok, B. K., and G. A. Campbell, "Two-phase simulation of tubular film-blowing of crystalline polymers," Int. Polym. Process. **7**, 240–247 (1992).

Bird, R. B., C. F. Curtiss, R. C. Armstrong, and O. Hassager, "Dynamics of polymeric liquids," in *Kinetic Theory*, 2nd ed. (Wiley, New York, 1987), Vol. 2.

Brent, R. P., "An algorithm with guaranteed convergence for finding a zero of a function," Comput. J. **14**, 422–425 (1971).

Cain, J. J., and M. M. Denn, "Multiplicities and instabilities in film blowing," Polym. Eng. Sci. **28**, 1527–1541 (1988).

Cantor, K., *Blown Film Extrusion: An Introduction* (Hanser, Munich, 2006).

Cherukupalli, S. S., "Online measurements of microstructure using Raman spectroscopy and structure-property relationships in blown film extrusion of polyolefins," Ph.D. thesis, Clemson University, 2004.

Cherukupalli, S. S., and A. A. Ogale, "Integrated experimental-modeling study of microstructural development and kinematics in a blown film extrusion process: Real-time Raman spectroscopy measurements of crystallinity," Plast. Rubber Compos. **33**, 367–371 (2004a).

Cherukupalli, S. S., and A. A. Ogale, "Online measurements of crystallinity using Raman spectroscopy during blown film extrusion of a linear low-density polyethylene," Polym. Eng. Sci. **44**, 1484–1490 (2004b).

Cherukupalli, S. S., S. E. Gottlieb, and A. A. Ogale, "Real time Raman spectroscopic measurement of crystallization kinetics and its effect on the morphology and properties of polyolefin blown films," J. Appl. Polym. Sci. **98**, 1740–1747 (2005).

Doufas, A. K., A. J. McHugh, and C. Miller, "Simulation of melt spinning including flow-induced crystallization. Part I. Model development and predictions," J. Non-Newtonian Fluid Mech. **92**, 27–66 (2000).

Doufas, A. K., and A. J. McHugh, "Simulation of film blowing including flow-induced crystallization. Model development and predictions," J. Rheol. **45**, 1085 (2001).

Han, C. D., and J. Y. Park, "Studies on blown film extrusion. II. Analysis of the deformation and heat transfer processes," J. Appl. Polym. Sci. **19**, 3277–3290 (1975).

Henrichsen, L. K., "Modeling of film blowing," M.S. thesis, University of Illinois at Urbana-Champaign, 2002.

Henrichsen, L. K., "Steady state modeling and dynamic analysis of film blowing," Ph.D. thesis, University of Illinois at Urbana-Champaign, 2006.

Henrichsen, L. K., A. J. McHugh, S. S. Cherukupalli, and A. A. Ogale, "Microstructure and kinematic aspects of blown film extrusion process: II. Numerical modeling and prediction of LLDPE and LDPE," Plast. Rubber Compos. **33**, 383–389 (2004).

Henrichsen, L. K., and A. J. McHugh, "Analysis of film blowing with flow-enhanced crystallization. Part. I. Steady-state behavior," Int. Polym. Process. **22**, 179–189 (2007).

Hindmarsh, A. C., "ODEPACK, a systematized collection of ODE solvers," in *Scientific Computing*, edited by R. S. Stepleman *et al.* (North-Holland, Amsterdam, 1983), pp. 55–64.

Hyun, J. C., H. Kim, J. S. Lee, S. Song, and W. W. Jung, "Transient solutions of the dynamics in film blowing processes," J. Non-Newtonian Fluid Mech. **121**, 157–162 (2004).

Lee, J. S., H.-S. Song, H. W. Jung, and J. C. Hyun, "Existence of optimal cooling conditions in the film blowing process," J. Non-Newtonian Fluid Mech. **137**, 24–30 (2006).

Liu, C.-C., "Studies of mathematical modeling and experimental on-line measurement techniques for the tubular film blowing process," M.S. thesis, University of Tennessee, Knoxville, 1991.

Liu, C.-C., "On-line experimental study and theoretical modeling of tubular film blowing," Ph.D. thesis, University of Tennessee, Knoxville, 1994.

Liu, C.-C., D. C. Bogue, and J. E. Spruiell, "Tubular film blowing. Part 2. Theoretical modeling," Int. Polym. Process. **10**, 230–236 (1995).

Luo, X.-L., and R. I. Tanner, "A computer study of film blowing," Polym. Eng. Sci. **25**, 620–629 (1985).

Maly, T., and L. R. Petzold, "Numerical methods and software for sensitivity analysis of differential-algebraic systems," Appl. Numer. Math. **20**, 57–79 (1996).

Patel, R. M., A. K. Doufas, and R. P. Paradkar, "Raman spectroscopy for spin line crystallinity measurements. II. Validation of fundamental fiber spinning models," J. Appl. Polym. Sci. **109**, 3398–3412 (2008).

Pearson, J. R. A., and C. J. S. Petrie, "The flow of a tubular film. Part 1. Formal mathematical representation," J. Fluid Mech. **40**, 1–19 (1970a).

Pearson, J. R. A., and C. J. S. Petrie, "The flow of a tubular film. Part 2. Interpretation of the model and discussion of the solutions," J. Fluid Mech. **42**, 609–625 (1970b).

Pearson, J. R. A., and C. J. S. Petrie, "A fluid-mechanical analysis of the film-blowing process," Plast. Polym. **38**, 85–94 (1970c).

Petrie, C. J. S., "Mathematical modeling of heat transfer in film blowing-case study," Plast. Polym. **42**, 259–264 (1974).

Petrie, C. J. S., "Mathematical modeling and the systems approach in plastic processing: The blown film process," Polym. Eng. Sci. **15**, 708–724 (1975).

Petrie, C. J. S., "Tubular film blowing-myths and science," in *Proceedings of the 6th European Conference on Rheology* (Institute of Polymeric Materials, University of Erlangen-Nurnberg, Germany, 2002), pp. 417–418.

Petzold, L. R., "A description of DASSL: A differential/algebraic system solver," in *Scientific Computing*, edited by R. S. Stepleman (North-Holland, Amsterdam, 1983), pp. 65–68.

Pirkle, J. C., and R. D. Braatz, "Dynamic modeling of blown film extrusion," Polym. Eng. Sci. **43**, 398–418 (2003).

Pirkle, J. C., and R. D. Braatz, "Comparison of the dynamic thin shell and quasi-cylindrical models for blown film extrusion," Polym. Eng. Sci. **44**, 1267–1276 (2004).

Schiesser, W. E., *The Numerical Method of Lines Integration of Partial Differential Equations* (Academic, San Diego, 1991).

Schiesser, W. E., "PDE boundary conditions from minimum reduction of the PDE," Appl. Numer. Math. **20**, 171–179 (1996).

Shin, D. M., J. S. Lee, H. W. Jung, and J. C. Hyun, "Multiplicity, bifurcation, stability and hysteresis in dynamic solutions of film blowing process," J. Rheol. **51**, 605–621 (2007).

Shrikhande, P., W. H. Kohler, and A. J. McHugh, "A modified model and algorithm for flow-enhanced crystallization—Application to fiber spinning," J. Appl. Polym. Sci. **100**, 3240–3254 (2006).

Silebi, C. A., and W. E. Schiesser, *Dynamic Modeling of Transport Process Systems* (Academic, San Diego, 1992), p. 409.

Yeow, Y. L., "Stability of tubular film flow: A model of the film blowing process," J. Fluid Mech. **75**, 577–591 (1976).

Yoon, K.-S., and C.-W. Park, "Stability of a blown film extrusion process," Int. Polym. Process. **14**, 342–349 (1999).

Yoon, K.-S., and C.-W. Park, "Stability of a two-layer blown film coextrusion," J. Non-Newtonian Fluid Mech. **89**, 97–116 (2000).

Ziabicki, A., *Fundamentals of Fiber Formation* (Interscience, New York, 1976).